Cellular/Molecular

Viral Transfer of Mini-Otoferlins Partially Restores the Fast Component of Exocytosis and Uncovers Ultrafast Endocytosis in Auditory Hair Cells of Otoferlin Knock-Out Mice

Margot Tertrais,[1] Yohan Bouleau,[1] Alice Emptoz,[2] Séverin Belleudy,[1] R. Bryan Sutton,[3] Christine Petit,[2,4] Saaid Safieddine,[2,5]* and Didier Dulon[1]*

[1]Neurophysiologie de la Synapse Auditive, Institut National de la Santé et de la Recherche Médicale, UMR 1120, Université de Bordeaux, 33076 Bordeaux, France, [2]Génétique et Physiologie de l'Audition, Institut National de la Santé et de la Recherche Médicale, UMR 1120, Institut Pasteur, 75015 Paris, France, [3]Department of Cell Physiology and Molecular Biophysics, Texas Tech University Health Sciences Center, Lubbock, Texas 99430, [4]Collège de France, 75005 Paris, France, and [5]Centre National de la Recherche Scientifique, 75016 Paris, France

Transmitter release at auditory inner hair cell (IHC) ribbon synapses involves exocytosis of glutamatergic vesicles during voltage activation of L-type $Ca_v1.3$ calcium channels. At these synapses, the fast and indefatigable release of synaptic vesicles by IHCs is controlled by otoferlin, a six-C2-domain (C2-ABCDEF) protein that functions as a high-affinity Ca^{2+} sensor. The molecular events by which each otoferlin C2 domain contributes to the regulation of the synaptic vesicle cycle in IHCs are still incompletely understood. Here, we investigate their role using a cochlear viral cDNA transfer approach *in vivo*, where IHCs of mouse lacking otoferlin (*Otof*$^{-/-}$ mice of both sexes) were virally transduced with cDNAs of various mini-otoferlins. Using patch-clamp recordings and membrane capacitance measurements, we show that the viral transfer of mini-otoferlin containing C2-ACEF, C2-EF, or C2-DEF partially restores the fast exocytotic component in *Otof*$^{-/-}$ mouse IHCs. The restoration was much less efficient with C2-ACDF, underlining the importance of the C2-EF domain. None of the mini-otoferlins tested restored the sustained component of vesicle release, explaining the absence of hearing recovery. The restoration of the fast exocytotic component in the transduced *Otof*$^{-/-}$ IHCs was also associated with a recovery of Ca^{2+} currents with normal amplitude and fast time inactivation, confirming that the C-terminal C2 domains of otoferlin are essential for normal gating of $Ca_v1.3$ channels. Finally, the reintroduction of the mini-otoferlins C2-EF, C2-DEF, or C2-ACEF allowed us to uncover and characterize for the first time a dynamin-dependent ultrafast endocytosis in IHCs.

Key words: calcium sensor; deafness; exocytosis; hair cells; otoferlin; ribbon synapses

Significance Statement

Otoferlin, a large six-C2-domain protein, is essential for synaptic vesicle exocytosis at auditory hair cell ribbon synapses. Here, we show that the viral expression of truncated forms of otoferlin (C2-EF, C2-DEF, and C2-ACEF) can partially rescue the fast and transient release component of exocytosis in mouse hair cells lacking otoferlin, yet cannot sustain exocytosis after long repeated stimulation. Remarkably, these hair cells also display a dynamin-dependent ultrafast endocytosis. Overall, our study uncovers the pleiotropic role of otoferlin in the hair cell synaptic vesicle cycle, notably in triggering both ultrafast exocytosis and endocytosis and recruiting synaptic vesicles to the active zone.

Introduction

Sound encoding into electrical nerve impulses by inner hair cell (IHC) ribbon synapses is a step crucial to normal hearing. Each of 10 to 20 active zones per IHC is able to drive the spiking rate of its corresponding afferent auditory nerve fiber up to the kilohertz range and maintains its firing rate at several hundred hertz during sustained sound stimulation (Kiang, 1965; Palmer and Russell, 1986; Taberner and Liberman, 2005). To faithfully achieve this

Received June 15, 2018; revised Oct. 24, 2018; accepted Nov. 2, 2018.

Author contributions: M.T., R.B.S., S.S., and D.D. designed research; M.T., Y.B., A.E., and S.B. performed research; M.T., Y.B., A.E., and D.D. analyzed data; M.T. wrote the first draft of the paper; M.T., C.P., S.S., and D.D. edited the paper; D.D. wrote the paper.

This work was supported by a grant from the Fondation Pour l'Audition (D.D.), European Commission Grant ERC-2011-ADG_294570, LabEx Lifesenses Grant ANR-10-LABX-65, and French government funds managed by the Agence Nationale de la Recherche (EargenCure).

*S.S. and D.D. contributed equally to this work.

The authors declare no competing financial interests.

Correspondence should be addressed to Didier Dulon at didier.dulon@inserm.fr.

https://doi.org/10.1523/JNEUROSCI.1550-18.2018

encoding process, synaptic vesicle release at the IHC active zones must occur with high temporal precision as well as reach and sustain an extremely high rate of exocytosis, which places an extraordinary demand on the molecular machinery responsible for vesicle recycling (for review, see Moser et al., 2006). Despite its great importance in maintaining membrane homeostasis and sustained vesicle release at the IHC active zone, the precise mechanism by which exocytosed vesicles are rapidly recycled through endocytosis remains largely unknown.

In CNS synapses, synaptotagmin I and II—proteins with one N-terminal transmembrane region and two C-terminal C2 domains (C2-A and C2-B)—are known to serve as essential calcium sensors for vesicle exocytosis and transmitter release (Chapman, 2008; Südhof, 2012). Although synaptotagmins are transiently expressed in immature spiking IHCs (before the onset of hearing in mice), these neuronal Ca^{2+} sensors are not involved in mature IHCs (Beurg et al., 2010). It is otoferlin, a large protein having six C2 domains (C2-ABCDEF) and a single transmembrane domain at its C-terminal end (Fig. 1), that serves as a Ca^{2+} sensor for vesicle exocytosis in cochlear (Roux et al., 2006; Michalski et al., 2017) and vestibular hair cells (Dulon et al., 2009). However, the precise molecular events by which each otoferlin C2 domain contributes to the synaptic vesicle cycle is still incompletely understood.

Otoferlin has also been suggested to have a role in vesicle clathrin-dependent endocytosis, based on its interaction with the AP-2 adaptor protein complex (Duncker et al., 2013; Jung et al., 2015; Selvakumar et al., 2017) and on a reduced membrane trafficking at the ribbon active zone in *Otof*$^{-/-}$ mice (Revelo et al., 2014). Different modes of endocytosis seem to coexist in IHCs because different kinetics for membrane retrieval have been observed: one fast (with a time constant of several hundreds of milliseconds; Neef et al., 2014; Vincent et al., 2014; Michalski et al., 2017) and one slow (with a 10–20 s time constant; Moser and Beutner, 2000; Beutner et al., 2001; Cho et al., 2011). Neither of these modes of endocytosis is likely sufficiently fast to support the extremely high rate of exocytosis occurring in IHCs. A much faster compensatory endocytosis, which remains to be identified, must take place in IHCs to maintain the active zone's original surface area and prevent depletion of vesicle pools.

Recent studies from invertebrate neuromuscular junctions (Watanabe et al., 2013a) and mouse hippocampal synapses (Watanabe et al., 2013b, 2014), using high-pressure freezing electron microscopy paired with optogenetic stimulation, showed that synaptic vesicles can be recycled extremely rapidly via clathrin-independent ultrafast endocytosis, with a time constant in the range of tens of milliseconds. Here, we examined whether such an ultrafast endocytosis, which has been shown to be dynamin and actin dependent (Watanabe et al., 2014; Delvendahl et al., 2016), occurs in mouse IHCs. Furthermore, we explored the role of various C2 domain combinations in IHC exocytosis/endocytosis by using an *in vivo* cochlear viral cDNA transfer of various mini-otoferlin constructs in mice lacking otoferlin (Fig. 1). We found that the viral expression of mini-otoferlins that contain the C-terminal C2-E and C2-F domains, induced a restoration of the fast component of synaptic vesicle exocytosis in *Otof*$^{-/-}$ IHCs but not the sustained component during repeated stimulations. Also, the reintroduction of these mini-otoferlins allowed us to uncover a novel ultrafast endocytosis mechanism in IHCs.

Materials and Methods

Viral vector constructs. The murine cDNA corresponding to the mini-*Otof* C2-EF (1896 bp; amino acids 1364–1996), C2-DEF (2763 bp; amino acids 960-1996), C2-ACDF (3465 bp), and C2-ACEF (3432 bp) domains of otoferlin were cloned into an AAV8.CB6.PI.rBG plasmid (p1045; Penn Vector Core; Fig. 1*A*). The C2-ACEF construct contains three disruptions: 125r394 (in amino acids) containing the C2-B domain, 946r1490 containing the C2-D domain, and 1695r1731 between the C2-E and C2-F domains. The C2-ACDF construct contains two disruptions: 125r394 containing the C2-B domain and 1110r1679 containing the C2-E domain. These mini-*Otof* C2-ACEF or C2-ACDF sequences were designed with a similar structure-based method developed for dysferlin (Llanga et al., 2017). Each C2 domains was analyzed by predicted β strands, potential Ca^{2+}-binding residues, C2-domain topology and length, and continuity of the hydrophobic packing in the core of the domain. Then, the otoferlin sequence was edited *in silico* by defining excision sites. The absolute boundaries for each of the six C2 domains of the mouse otoferlin protein were selected based on several factors. The approximate location of each C2 domain could be delineated based on the output from the SMART database. This server (http://smart.embl-heidelberg.de/) can identify the presence of each domain; however, the structural boundaries are not necessarily clear. With the approximate boundaries defined, each domain was aligned and sorted against an extensive library of known type 1 and type 2 C2 domain ferlins. The resulting phylogenetic tree sorted each otoferlin C2 domain according to its most likely topology. Once the topology was defined, each of the eight β-strands was located by aligning the known "in-out-in-out" periodicity characteristic of C2-domain β-strands. This time-consuming method reduces the risk of misdefining a large loop insertion as a α- or β-secondary structure that may actually be unique to an individual C2 domain. Once the accurate boundaries of each C2 were established, two mini-*Otof*s were constructed by excluding individual domains and linker regions. Only C2-A, the central FerA domain, C2-F, and the transmembrane span were left intact. Two shorter genes that could be accommodated within an adeno-associated virus (AAV) were constructed using these rules: *Otof* C2-ACEF and *Otof* C2-ACDF. The coding sequence of each mini-*Otof* was synthesized (GeneCust Europe), subcloned into an AAV2 genome, and packaged in an AAV8 capsid as described by Emptoz et al. (2017).

The expressions of these different mini-*Otof* genes were all driven by the CB6 promoter (1 kb). Because of the 4.8 kb packaging limit of the AAV8 vector, only the sequence of the mini-*Otof* C2-EF was followed by an internal ribosome entry site (IRES; 0.6 kb) and the eGFP reporter gene (0.7 kb), allowing a direct monitoring of transfected IHCs (Fig. 1*B*). The transduction of mini-*Otof* C2-EF and C2-DEF was assessed by confocal immunomicroscopy, whereas the expression of mini-*Otof* C2-ACEF and C2-ACDF was determined by RT-PCR (see below, RT-PCR to detect C2-ACEF and C2-ACDF transcripts).

Round window membrane injection. The AAV8 vector containing the mini-*Otof* sequences was injected in the cochlea at a titer of 3.21×10^{13} genome copies (gc)/ml, and the AAV8.CB6.eGFP with no inserted mini-otoferlin gene was used as control at a titer of 3.34×10^{13} gc/ml. Protocols were approved by the Animal Care and Use Committee of the Institut Pasteur and the University of Bordeaux. Intracochlear viral transduction was performed as described previously (Akil et al., 2015; Emptoz et al., 2017; Dulon et al., 2018). Mice were anesthetized using hypothermia exposure. A left postauricular incision was made to expose the otic bulla and to visualize the cochlea. A glass micropipette containing 1 μl of AAV vector preparation was inserted through the round window membrane and injected into the cochlea. The pipette was removed, the hole in the membrane was covered with connective tissue, and the incision was sealed with biological glue (3M Vetbond). Standard postoperative care was applied.

Auditory brainstem responses. To record auditory brainstem responses (ABRs; which represent the sound-evoked synchronous firing of the auditory cochlear nerve fibers) as well as distortion product otoacoustic emissions [DPOAEs; which reflect the amplification provided by outer hair cells (OHCs)], mice were anesthetized with intraperitoneal injection of a mixture of xylazine (6 mg/ml, Rompun catalog #KP091XW, Centravet) and ketamine (80 mg/ml, Virbac catalog #4C14, Centravet) diluted in physiological saline. The mouse body temperature was kept constant at 37°C. For stimulus generation and data acquisition, we used a TDT

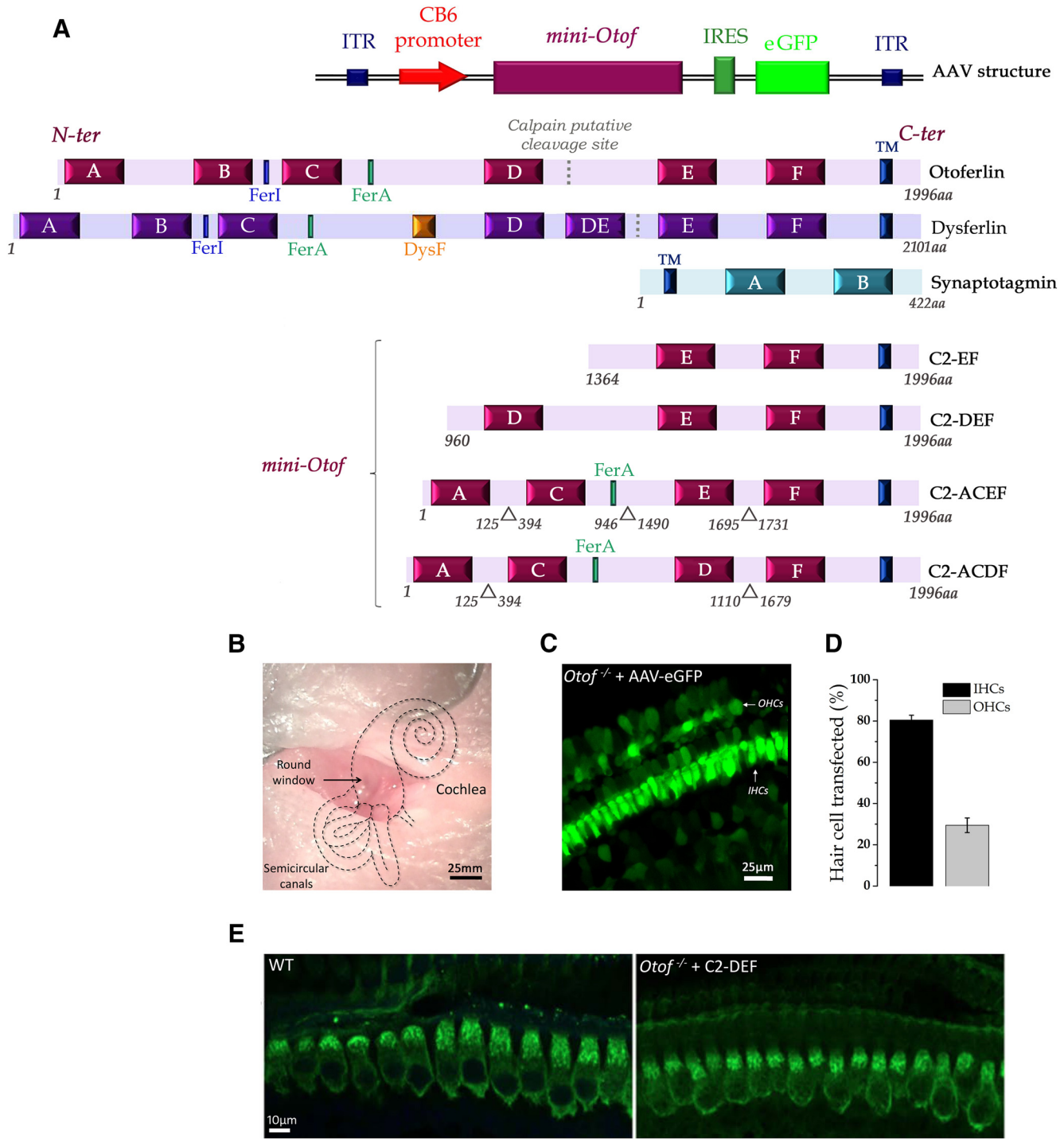

Figure 1. Comparative structure of the native otoferlin and the four different mini-otoferlins inserted in the AAV vector to evaluate their role in hearing and IHC exocytosis. ***A***, Otoferlin is a large protein (~2000 amino acids) that contains a single TM domain at its C-terminal part, a FerA domain, and six C2 domains (C2-A to C2-F) that potentially bind calcium (Ca^{2+}) and interact with phospholipids. Dysferlin, a dystrophy-associated Fer-1-like protein, contains seven C2 domains, a FerA domain, and a DysF domain. The dotted lines in the otoferlin and dysferlin sequences indicate a putative calpain cleavage site (Lek et al., 2012; Redpath et al., 2014). Synaptotagmins, the major Ca^{2+} sensors in CNS synapses, which are absent in IHCs synapses (Beurg et al., 2010), contain only two C2 domains. Note that in humans, a short isoform of otoferlin with three C2-domains (C2-DEF) and a FerA domain with unknown function has been identified (Yasunaga et al., 1999). The putative function of these truncated mini-otoferlins, C2-EF and C2-DEF, in IHC exocytosis remains unknown. Also, two abridged otoferlin-like containing C2-ACEF or C2-ACDF constructs (~30% smaller than the native otoferlin) were tested. The AAV8 sequence contains a promoter CB6 that allows the expression of the short otoferlins (C2-EF, C2-DEF, C2-ACEF or C2-ACDF domains) and the eGFP reporter (only for C2-EF) in IHCs. (ITR as Inverted Terminal Repeat sequences). ***B***, AAVs are injected *in vivo* through the round window of the cochlea at P1–P3. ***C***, For C2-EF, the successful AAV infection of IHCs was verified with the fluorescent reporter eGFP. ***D***, Rates of transfection for IHCs and OHCs, respectively. Error bars indicate SE. ***E***, The expression of the mini-otoferlin C2-DEF in *Otof*$^{-/-}$ IHCs was verified by immunoconfocal imaging with a C-terminal otoferlin antibody. Note that the expression of C2-DEF was similar to that of the native otoferlin in WT IHCs.

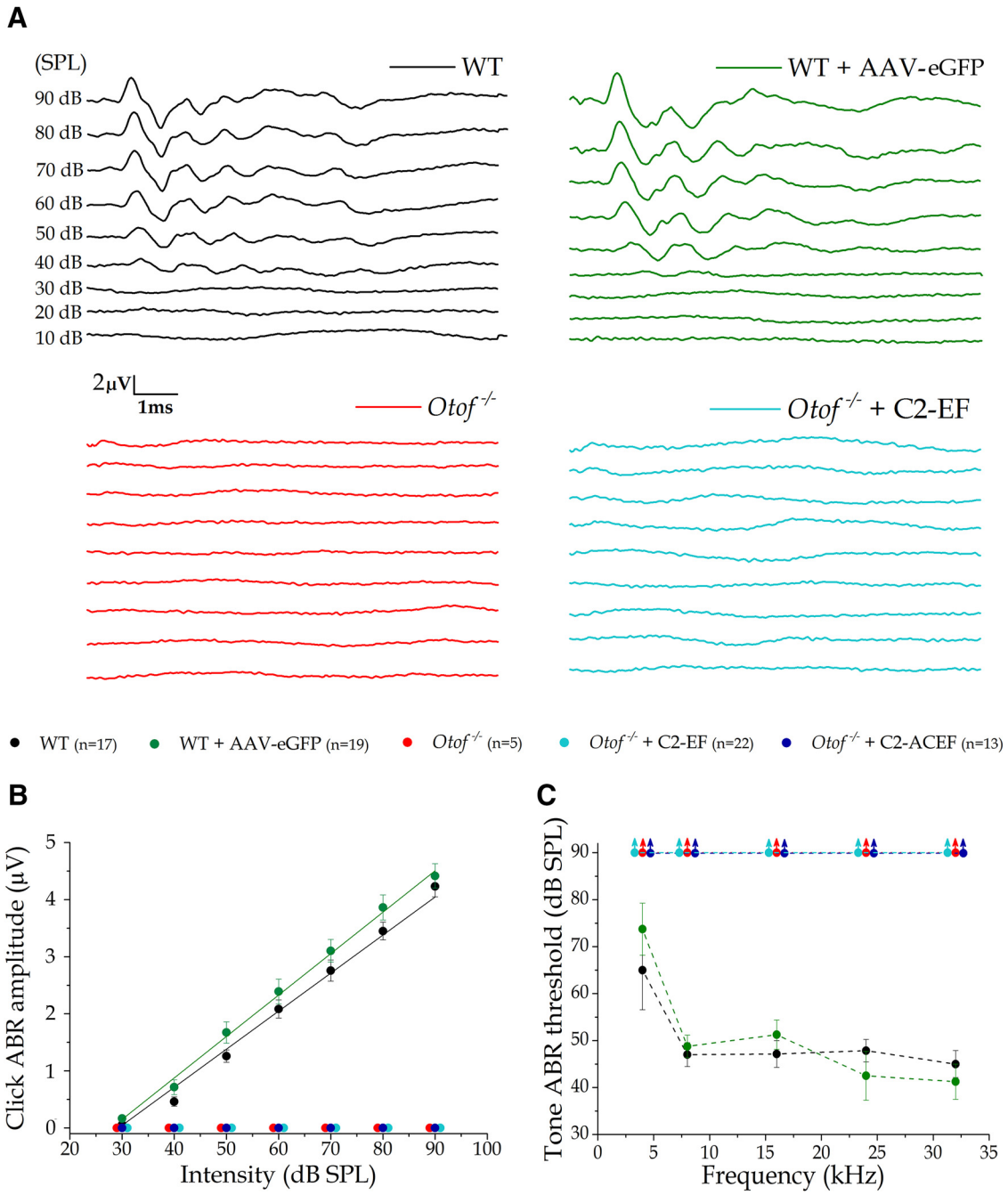

Figure 2. Viral transfer of mini-otoferlins to IHCs failed to restore ABRs in *Otof*$^{-/-}$ mice. The auditory function was tested 2 and 3 weeks (P15–P21) after the viral injection. ***A***, Example of click-ABR waves at different sound intensities (10–90 dB SPL) in WT (black trace) and WT mice injected with AAV8-eGFP (sham-injected, green trace). Note the absence of ABR waves in both noninjected *Otof*$^{-/-}$ mice (red trace) and AAV8–C2-EF-IRES-eGFP-injected mice (light blue trace). ***B***, ***C***, Mean ABR wave I amplitude as a function of sound intensities (***B***) and tone ABR thresholds at sound frequencies from 4 to 32 kHz (***C***) also indicated the absence of ABR waves in injected *Otof*$^{-/-}$ mice with Otof-C2-EF (light blue) or Otof-C2-ACEF (dark blue). Note that similar results were obtained with the other mini-otoferlins, C2-DEF or C2-ACDF (not shown for clarity). Error bars indicate SE.

RZ6/BioSigRZ system (Tucker-Davis Technologies). ABR signals were averaged after the presentation of a series of 512 stimulations. ABR thresholds were defined as the lowest stimuli for recognizable waves I and II. The amplitude of ABR wave I was estimated by measuring the voltage difference between the positive and negative peaks of wave I. Pure-tone stimuli were used at frequencies of 4, 8, 16, 24, and 32 kHz. Sound intensities of 10 to 90 dB SPL, in 10 dB step, were tested (Fig. 2).

Tissue preparation of the organ of Corti. Experiments were performed in accordance with the guidelines of the Animal Care Committee of the European Communities Council Directive (86/609/EEC) and were approved by the ethics committee of the University of Bordeaux (Animal Facility Agreement No. C33-063-075). All mice (C57BL6 of either sex) were anesthetized by intraperitoneal injection of a xylazin (6 mg/ml) and ketamine (80 mg/ml) mixture (Rompun, catalog #KP091XW; Vibrac, catalog #4C14) diluted in physiological saline. Electrophysiological recordings from IHCs were obtained in whole-mount organ of corti (OC) from mice at postnatal day 15 (P15)–P21, that is, after the onset of hearing. The OC was freshly dissected under binocular microscopy in an extracellular solution maintained at 4°C containing the following (in mM): 135 NaCl, 5.8 KCl, 1.3 $CaCl_2$, 0.9 $MgCl_2$, 0.7 NaH_2PO_4, 5.6 glucose, 2 Na pyruvate, and 10 HEPES, pH 7.4, 305 mOsm. The OC was then placed in a recording chamber and visualized under a Nikon 60× water

immersion (WI) objective (CFI Fluor 60× Near InfraRed, Working Distance 2.0mm and Numerical Aperture 1) attached to an upright Nikon FN1 microscope coupled to a C2 confocal fluorescent imaging system. The extracellular solution was complemented with 0.25 μM of apamin (Latoxan, catalog #L8407) and 1 μM of XE-991 (Tocris Bioscience, catalog #2000) to block SK channels and KCNQ4 channels, respectively. The external Ca^{2+} concentration was increased from 1.3 to 5 mM to enhance the amplitude of Ca^{2+} currents to levels nearby body temperature. All experiments were performed at room temperature (22°C–24°C).

Patch-clamp recording and capacitance measurement. All IHC recordings were performed in the 20–40% normalized distance from the apex, an area coding for frequencies ranging from 8 to 16 kHz, using an EPC10 amplifier controlled by Patchmaster pulse software (HEKA Elektronik). For the mini-*Otof* C2-EF experiments, only eGFP-expressing IHCs were recorded. For the other mini-*Otof* experiments, in the absence of eGFP fluorescent signaling, IHCs were randomly recorded in the tissue preparation. Patch pipettes were pulled with a micropipette puller (P-97 Flaming/Brown; Sutter Instrument) and fire polished with an MF-830 microforge (Narishige) to obtain a resistance range of 2 to 4 MΩ. Patch pipettes were filled with an intracellular cesium-based solution containing the following (in mM): 145 CsCl, 1 $MgCl_2$, 5 HEPES, 1 EGTA, 20 TetraEthylAmmonium chloride, 2 ATP, and 0.3 GTP, pH 7.2, 300 mOsm. Changes in cell membrane capacitance (ΔC_m) were used to monitor fusion of synaptic vesicles during exocytosis. The C_m was measured accordingly to the Lindau and Neher (1988) technique by using the lock-in amplifier Patchmaster software (HEKA) and applying a 1 kHz command sine wave (20 mV amplitude) at holding potential (−80 mV) before and after the pulse experiment. Because recording conditions can greatly influence capacitance measurements, only IHC patch-clamp recordings with low series resistance below 10 mΩ and a maximum leak current of 25 pA (at $V_h = -80$ mV) were considered in the present study.

Voltage stimulation. Three protocols were used. First, readily releasable pool (RRP) exocytosis was recorded during a protocol in which IHCs were depolarized from −80 to −10 mV with increasing durations from 5 to 40 ms in 5 ms increments. Second, RRP exocytosis was also recorded during a protocol of five consecutive stimulations of 20 ms each, separated by 100 ms interpulses. Third, a protocol probing the replenishment of the synaptic zone in vesicles where IHCs were depolarized during a train of 100 ms pulses from −80 to −10 mV was used.

Intracellular Ca^{2+} uncaging. To trigger a fast increase in intracellular Ca^{2+} concentration from the caged Ca^{2+} chelator DM-Nitrophen (Interchim, catalog #317210), we used 100 ms brief flashes from a 365 nm UV light source delivered by a Mic-LED-365 (350 mW; Prizmatix). The UV LED was directly connected to the epi-illumination port at the rear of the upright Nikon FN1 microscope and illumination focalized through the 60× objective (CFI Fluor 60× W NIR, WD = 2.0 mm, NA = 1). Hair cells were loaded with the following (in mM[SCAP]): 145 CsCl, 5 HEPES, 20 TEA, 10 DM-Nitrophen, and 10 $CaCl_2$. After rupture of the patch, we waited systematically for 2 min at a holding potential of −70 mV to load and equilibrate the cells with the intrapipette solution. Upon UV photolysis, the changes in $[Ca^{2+}]_i$, continuously measured with a C2 confocal system and NIS-Elements imaging software (Nikon) coupled to the FN1 microscope, reached nearly a mean maximum value of 20 ± 5 μM within 15–20 ms (Michalski et al., 2017), a value that was not different between wild-type (WT) and $Otof^{-/-}$ IHCs, as shown previously by Vincent et al. (2015).

Dyngo-4a application. For each set of experiments, during voltage stimulation or Ca^{2+} uncaging, control recordings (I_{Ca} and ΔC_m) were obtained in the same organ of Corti by first bathing in normal perilymph and then adding 30 μM of Dyngo-4a (dynamin inhibitor from Abcam, catalog #ab120689) for 20 min before recording its effect on I_{Ca} and ΔC_m.

Immunostaining and confocal microscopy. Rapidly dissected P15–P21 mouse cochleae were fixed with cold 4% paraformaldehyde at 4°C overnight. Once washed with cold PBS, they were decalcified for several hours in 10% EDTA buffered with PBS. After PBS washing, whole bones were removed and Reissner and tectorial membranes were carefully removed to open scala media and allow efficient antibodies access to the OC. Tissues were first incubated with PBS containing 30% normal horse serum and 0.5% Triton X-100 for 1 h at room temperature. Then, they were incubated with primary antibodies diluted with PBS (1:200) containing 5% horse serum and 0.1% Triton X-100.

Synaptic ribbons were labeled with a goat polyclonal anti-CtBP2 (Santa Cruz Biotechnology, catalog #SC-5966; RRID:AB_2086774); the otoferlin C-ter part was labeled with a rabbit polyclonal antibody (Roux et al., 2006). Once washed with PBS, tissues were incubated with a suitable mix of secondary antibodies at 1:500 for 2 h at room temperature: donkey anti-rabbit Alexa 488 (Abcam, catalog #ab150061; RRID: AB_2571722) and donkey anti-goat Fluoprobes 547H (Interchim, catalog #FP-SB2110; RRID:AB_2744533). To identify and localize the hair cells in our surface preparation of the organ of Corti, F-actin (highly concentrated in the hair cell stereocilia) was stained using tagged Phalloidin Fluoprobe 405 (1:200; Interchim, catalog #FP-CA9870). To better visualize the ribbons and otoferlin in our images, the fluorescent channel of F-actin labeling was not shown.

After PBS washing, OC surface preparations were mounted on Superfrost slides in ProLong Antifade mounting medium (Invitrogen, catalog # P7481) and kept in the dark at −20°C until observation. All comparative immunoreactions were performed simultaneously on the same days in rigorously identical conditions.

Confocal imaging was performed with a Leica SP8 confocal laser-scanning microscope (Bordeaux Imaging Center) with a 63× oil-immersion objective (NA = 1.4) and white light laser (470 to 670 nm). Phalloidin was imaged using a diode laser at 405 nm also mounted on the microscope. Stack images were acquired with the following parameters: laser power, 60%; scan rate, 700 Hz; scans averaged per *XY* section, four; step size, 800 nm; pixel size, 103 nm, giving an *XY* image size of 53 × 53 μm (512 × 512 pixels). Images were analyzed with ImageJ software (W. S. Rasband, NIH).

RT-PCR to detect C2-ACEF and C2-ACDF transcripts. Two organ of Corti apical turns from either P50 injected with otoferlin C2-ACEF or C2-ACDF construct were freshly dissected and stored in separate low-DNA-binding tubes containing l μl of RNase inhibitor (Amresco, catalog #E633) maintained in dry ice. Total RNA was extracted from tissues using the RNAzol protocol (Molecular Research Center, catalog #RN 190). mRNA were purified using the Dynabeads mRNA Purification Kit (ThermoFisher Scientific, catalog # 61006) and reverse transcribed to cDNA by using the oligodT primers linked to the magnetic beads and AffinityScript Multiple Temperature Reverse Transcriptase (Stratagene, catalog #600107). Reverse transcription was performed at 37°C overnight. Specific PCR amplification was performed by using 0.45 μg of cDNA and Herculase II Fusion DNA Polymerase (Stratagene, catalog #600677). Specific sense and antisense primers (Eurofins Genomics) are summarized in Table 1.

Table 1. Sense and antisense primers used

Name of primer	Primer sequence (5′–3′)	Product size (bp) for C2-ACEF	Product size (bp) for C2-ACDF
231s	gatagggaccttctgcatgg	454	454
1494as	gaagacgacctgctcattcc		
1478s	atgagcaggtcgtcttcac	1142	1142
2720 as	ggcataggcgatacgtttgt		
1478s	atgagcaggtcgtcttcac	1146	
4563as	gatgtcggtcttgcctaact		
1478s	atgagcaggtcgtcttcac		1341
2919as	ggcttgcttcttggtgtag		

Data analysis. Data were analyzed using ImageJ, Patchmaster (HEKA Elektronik), and Origin 9.1 (OriginLab). Statistical analyses were performed using independent two-sample Student *t* tests and, for multiple comparisons, either one-way ANOVA (two-way ANOVA in the case of Fig. 3*B*,*C*,*G*) followed by Tukey's *post hoc* test for normally distributed data (Shapiro test) or the nonparametric Kruskal–Wallis test followed by Dunn's test for not normally distributed data. Means are expressed as ±SEM. In the figures, asterisks indicate statistical significance with $p < 0.05$. A statistical *F* test was used to compare the exocytotic curve efficiency in Figure 3*E*.

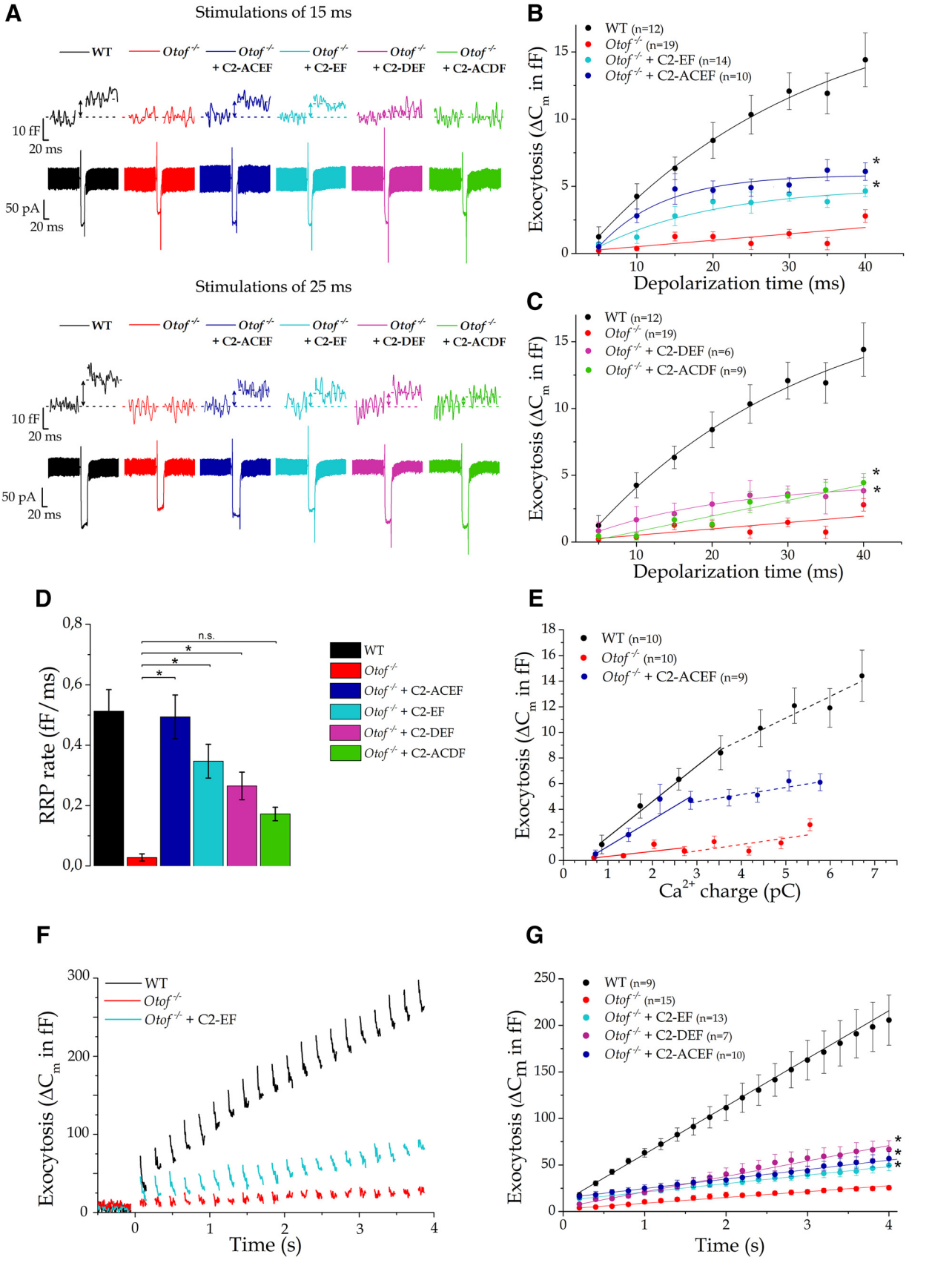

Figure 3. Mini-*Otof* constructs partially restore RRP exocytosis but not its vesicle resupply in P15–P21 *Otof*$^{-/-}$ mice. ***A***, Example traces of vesicular exocytosis (ΔC_m) and Ca^{2+} currents in IHCs triggered by 15 and 25 ms depolarizing steps from −80 to −10 mV in WT, *Otof*$^{-/-}$, and C2-ACEF-, C2-EF-, C2-DEF-, and C2-ACDF-injected *Otof*$^{-/-}$ mice. ***B***, Comparative kinetics of RRP exocytosis (depolarizing steps from −80 to −10 mV with increasing duration from 5 to 40 ms) for *Otof*-C2-ACEF-treated (dark blue) and C2-EF-treated (light-blue) *Otof*$^{-/-}$ IHCs. ***C***, RRP kinetics in C2-DEF (purple) and C2-ACDF (green). For ***B*** and ***C***, note a significant restoration of the exocytotic response compared with sham *Otof*$^{-/-}$ IHCs. *$p < 0.05$ (two-way ANOVA). Kinetics were best fitted with a single exponential with $R^2 > 0.94$ except for *Otof*-C2-ACDF and *Otof*$^{-/-}$. ***D***, Comparative rate of RRP exocytosis obtained by fitting with a linear function the first (*Figure legend continues.*)

Results

Viral transfer of mini-*Otof* cDNAs in hair cells lacking otoferlin

A single intracochlear viral injection of various AAV8 vectors containing different mini-otoferlin cDNA constructs (mini-*Otof*s) was performed in WT control mice and in mice lacking otoferlin (*Otof*$^{-/-}$ mice) on P1–P3 (Fig. 1*A*,*B*). Four mini-*Otof*s were designed and tested with regard to the following criteria: first, a synaptotagmin-like structure, that is, a mini-*Otof* containing only two C2 domains (C2-EF) attached to the C-terminal transmembrane domain; second, a structure similar to the short human otoferlin isoform, that is, containing the three last C-terminal C2 domains (C2-DEF) but lacking the FerA domain (Yasunaga et al., 2000); and third, two predicted abridged otoferlin-like containing C2-ACEF or C2-ACDF domain, designed using 3D structural modeling similar to that for nanodysferlin (Llanga et al., 2017).

The rate of hair cell transduction efficacy of the mini-*Otof* C2-EF-IRES-eGFP was first evaluated on postnatal days P15–P21 by counting eGFP-expressing hair cells (Fig. 1*C*,*D*). It is to be noted that to avoid a possible inhibitory effect of eGFP on the function of mini-C2-EF otoferlin, as observed previously when eGFP is attached to Syt 1 (Han et al., 2005), we added an IRES between the two coding sequences in the viral vector (Fig. 1*A*). This IRES sequence allowed then a separate expression of the mini-*Otof* C2-EF and eGFP under the CB6 promoter. We found that, all along the cochlear partition, the eGFP transduction was essentially associated with the sensory hair cells of the organ of Corti, with a much higher rate for IHCs compared to OHCs: 80.4 ± 2.3% and 29.5 ± 3.5%, respectively (unpaired *t* test, $p < 10^{-4}$; $n = 22$ cochleae; Fig. 1*D*). It is to be noted that the eGFP transduction in IHCs reached a higher percentage (above 90%) at the apical portion of the organ of Corti. In addition, the expression of the mini-*Otof*s C2-EF and C2-DEF in *Otof*$^{-/-}$ hair cells was directly assessed under confocal immunofluorescence microscopy at P15–P21 by using a specific antibody against the C terminal of otoferlin (Roux et al., 2006). At the apical turn of the injected cochlea, where most of electrophysiological recordings were performed, an average of 95 ± 5% of IHCs were found to express the mini-*Otof*s C2-EF ($n = 3$ mice) and C2-DEF ($n = 14$ mice). The subcellular distribution of these mini-*Otof* proteins was similar to that of the native otoferlin in wild-type mice, with a preferential higher expression in the basolateral area of IHCs where the ribbon synapses are located (Fig. 1*E*). Because the C2-ACEF and C2-ACDF constructs contain various disruptions in their encoding amino acid sequences (see Materials and Methods), rendering their immunodetection impossible with the various otoferlin antibodies currently in our hands, their expression in the organ of Corti was positively assessed at the mRNA level by RT-PCR (see Materials and Methods; data not shown).

Absence of auditory function recovery by cochlear injection of mini-*Otof* cDNAs

Mice lacking otoferlin (*Otof*$^{-/-}$ mice) are profoundly deaf due to a defect in synaptic vesicle release at the IHC ribbon synapse (Roux et al., 2006; Fig. 2). Measurements of ABRs were performed to evaluate a possible recovery in auditory function in AAV8-mini-*Otof*-injected *Otof*$^{-/-}$ mice. As a sham, we first verified that cochlear injection of AAV8-eGFP not containing the mini-*Otof* cDNAs did not affect hearing sensitivity of WT mice (Fig. 2*A*, green trace). The input–output function (click ABR-wave-I amplitude as a function of sound intensity; Fig. 2*B*) and the thresholds at different frequencies were similar between control WT sham-injected mice and WT noninjected mice (Fig. 2*C*). Furthermore, we found that hearing thresholds of WT mice were not affected for up to 3 months after cochlear injection, indicating the innocuity of the surgical and viral procedures, as reported previously (Emptoz et al., 2017; Dulon et al., 2018). The DPOAEs of WT mice, which probe the activity of OHCs, also remained unaffected by viral injections (data not shown). Cochlear injection of the various AAV8-mini-*Otof*s tested, C2-EF ($n = 22$ mice), C2-DEF ($n = 42$ mice), C2-ACEF ($n = 13$ mice), C2-ACDF ($n = 8$ mice), and C2-ACEF together with C2-ACDF ($n = 5$ mice), did not rescue the hearing phenotype in *Otof*$^{-/-}$ mice. These mice were tested for up to 3 months after injection. These results suggested that the cochlear injection of the various mini-*Otof*s tested did not restore normal synaptic exocytotic properties of *Otof*$^{-/-}$ IHCs.

Viral transfer of mini-*Otof*s in *Otof*$^{-/-}$ IHCs partially restores exocytosis of the readily releasable pool of vesicles but not its vesicle resupply

Although the measurement of auditory evoked potential (ABRs) is a good method to determine the overall integrity of the auditory system, this method is not precise enough to detect subtle changes in auditory function, notably those associated with certain synaptopathies produced by noise exposure and aging, which are thus classified as "hidden hearing loss" (Liberman, 2017). In this context, and in a reverse way, it is possible that subtle synaptic recovery after mini-*Otof* injections in *Otof*$^{-/-}$ mice cannot be detected in ABRs recordings. To assess whether IHC exocytosis was somewhat improved in mini-*Otof*-injected *Otof*$^{-/-}$ mice, we directly recorded IHCs using whole-cell patch-clamp experiments. The study of the presynaptic exocytotic function in IHCs was performed at P15–P21 in organ of Corti explants dissected either from WT (*Otof*$^{+/+}$) or *Otof*$^{-/-}$ mice injected with various AAV8-mini-*Otof*s (Fig. 1). All IHC patch-clamp recordings were performed in the 20–40% normalized distance from the apex, an area encoding sound frequencies ranging from 8 to 16 kHz.

First, we controlled the innocuity of the viral construct on IHC exocytosis. Recordings from P15–P21 WT IHCs of the cochlea injected with AAV8-eGFP (mice with no inserted mini-*Otof* are sham-injected mice) displayed similar exocytotic responses as

←

(*Figure legend continued.*) four time– data points of the kinetics shown in Figure 4, *B* and *C* (linear slope in femtofarad per millisecond). The expression of the mini-*Otof* constructs C2-ACEF, C2-EF, and C2-DEF allowed a significant increase in the rate of exocytosis compared with sham-injected *Otof*$^{-/-}$. *$p < 0.05$ (one-way ANOVA; see individual *p* values in Table 2). ***E***, Ca^{2+} efficiency of RRP exocytosis ($\Delta C_m/Q_{Ca}$) where the loading charge in Ca^{2+} (Q_{Ca}) was obtained by integrating the Ca^{2+} current evoked during a voltage step from −80 to −10 mV for different brief pulses lasting 5, 10, 15, and 20 ms (full line). The slope of *Otof*-C2-ACEF IHCs was not significantly different of the WT slope (2.77 ± 0.21 and 2.09 ± 0.28 fF/pC, respectively; *F* test with $F = 2.18$ and $p = 0.23$), which is larger than in *Otof*$^{-/-}$ mice (0.39 ± 0.20 fF/pC; $p = 5.8\ 10^{-3}$). For longer pulses (25, 30, 35, and 40 ms; dashed lines), exocytosis Ca^{2+} efficiency ($\Delta C_m/Q_{Ca}$) in *Otof*-C2-ACEF IHCs is decreased, with a slope similar to that for noninjected *Otof*$^{-/-}$ mice (0.56 ± 0.14 and 0.50 ± 0.30 fF/pC, respectively; *F* test with $F = 0.015$ and $p = 0.98$). ***F***, To evaluate the replenishment of the IHC active zone in vesicles, exocytosis was recorded during a train of 100 ms pulses from −80 to −10 mV, each stimulation separated by 100 ms. Examples of exocytotic traces of vesicular recruitment in control WT, *Otof*$^{-/-}$, and *Otof*-C2-EF-treated IHCs. ***G***, Comparative mean recruitment in *Otof*-C2-EF-, *Otof*-C2-DEF-, and *Otof*-C2-ACEF-treated IHCs. Note that in *Otof*$^{-/-}$ IHCs (red), the vesicles recruitment is severely impaired. When mini-*Otof* constructs are expressed in *Otof*$^{-/-}$ IHCs, the vesicle supply is only slightly, but significantly, restored compared to *Otof*$^{-/-}$ (two-way ANOVA, $p = 4.3\ 10^{-8}$; Tukey's *post hoc* test, $p < 10^{-4}$ for each as indicated by the asterisks), except for *Otof*-C2-ACDF (data not shown; $p = 0.16$).

Table 2. Summary of exocytosis properties (with *p* values indicating individual comparison with *Otof*$^{-/-}$)

	Function	WT	*Otof*$^{-/-}$ + C2-EF	*Otof*$^{-/-}$ + C2-DEF	*Otof*$^{-/-}$ + C2-ACEF	*Otof*$^{-/-}$ + C2-ACDF	*Otof*$^{-/-}$
Fig. 3*D*, one-way ANOVA, $p = 1.15\ 10^{-10}$	RRP rate (fF/ms)	0.51 ± 0.07 ($n = 12$)	0.35 ± 0.06 ($n = 14$) *$p = 2.2\ 10^{-5}$	0.27 ± 0.05 ($n = 6$) *$p = 0.047$	0.49 ± 0.07 ($n = 10$) *$p = 2.7\ 10^{-8}$	0.17 ± 0.02 ($n = 9$) $p = 0.308$	0.028 ± 0.012 ($n = 19$)
Fig. 3*E*, *F* test	RRP Ca^{2+} efficiency (fF/pC; full line)	2.77 ± 0.21 ($n = 10$)	1.49 ± 0.23 ($n = 10$) $p = 0.058$	0.47 ± 0.12 ($n = 6$) $p = 0.97$	2.09 ± 0.28 ($n = 9$) *$p = 0.018$	0.50 ± 0.24 ($n = 9$) $p = 0.92$	0.39 ± 0.20 ($n = 10$)
Fig. 4*C*, one-way ANOVA, $p = 1.35\ 10^{-3}$	I_{Ca} total (pA)	205 ± 13 ($n = 13$)	204 ± 7 ($n = 20$) *$p = 0.006$	207 ± 9 ($n = 7$) *$p = 0.019$	203 ± 7 ($n = 10$) *$p = 0.025$	202 ± 7 ($n = 10$) *$p = 0.022$	159 ± 14 ($n = 16$)
Fig. 4*D*, Kruskal–Wallis, $p = 1.5\ 10^{-6}$	Fast I_{Ca} inactivation (pA)	20.2 ± 4.0 ($n = 12$)	11.6 ± 2.7 ($n = 19$) $p = 0.249$	18.7 ± 3.1 ($n = 7$) *$p = 0.030$	8.1 ± 3.2 ($n = 10$) $p = 0.999$	0.6 ± 0.4 ($n = 10$) $p = 0.999$	5.0 ± 1.8 ($n = 17$)

* indicates significantly different with $p < 0.05$.

P15–P21 WT IHCs from noninjected cochleae. Indeed, for a 15 ms voltage step, from −80 to −10 mV, AAV8-eGFP-transduced IHCs showed a mean capacitance jump of 6.0 ± 1.4 fF ($n = 6$), a value comparable to that for WT IHCs from noninjected mouse cochleae (6.7 ± 1.0 fF; $n = 6$; unpaired *t* test, $p = 0.71$; data not shown). We also found no significant difference in the exocytotic responses between IHCs from WT sham-injected and WT noninjected mice for longer and repetitive depolarizing steps that involved vesicle recruitment (data not shown). As expected, we observed no rescue effect on exocytosis in *Otof*$^{-/-}$ IHCs. For a 15 ms voltage step, from −80 to −10 mV, *Otof*$^{-/-}$ IHCs transduced with AAV8-eGFP showed a mean capacitance jump of 0.83 ± 0.5 fF ($n = 6$), a value comparable to that for *Otof*$^{-/-}$ IHCs from noninjected mouse cochleae (1.5 ± 0.4 fF; $n = 13$; unpaired *t* test, $p = 0.38$). Because IHCs from sham-injected mice displayed exocytotic properties similar to those of IHCs from noninjected mice, these data were combined and used as controls. Controls were named WT or *Otof*$^{-/-}$ in the rest of the study.

Conversely, recordings from *Otof*$^{-/-}$ IHCs of the cochleae injected with AAV-*Otof*-C2-EF-IRES-eGFP displayed a partial rescue of exocytosis when stimulated with brief depolarization impulses lasting <20 ms (Fig. 3*A*,*B*,*D*). These brief voltage impulses are believed to mobilize the RRP of vesicles at the active zones of the IHCs (Moser and Beutner, 2000; Michalski et al., 2017). For a 25 ms impulse from −80 to −10 mV, exocytosis in *Otof*-C2-EF-transduced IHCs, directly visualized with eGFP fluorescence, averaged 3.8 ± 0.8 fF ($n = 14$; from six mice issued from three different litters), a value significantly larger than that for littermate noninjected and sham (control) *Otof*$^{-/-}$ mice (1.5 ± 0.4 fF; one-way ANOVA, $p = 2.25\ 10^{-10}$; *post hoc* Tukey's test, $p = 0.045$) but significantly smaller than that for control WT IHCs (10.3 ± 1.4 fF; one-way ANOVA, *post hoc* Tukey's test, $p = 4.6\ 10^{-6}$; Fig. 3*A*–*C*). The kinetics of exocytosis *Otof*-C2-EF-transduced IHCs were significantly higher than in *Otof*$^{-/-}$ IHCs (two-way ANOVA, $p = 6.8\ 10^{-13}$; *post hoc* Tukey's test, $p = 1.8\ 10^{-8}$; Fig. 3*B*).

A similar partial rescue of exocytosis was obtained in *Otof*$^{-/-}$ IHCs from *Otof*-C2-DEF virus-injected cochlea (Fig. 3*A*–*C*; data from four mice of three different litters). Note that in this latter set of experiments with *Otof*-C2-DEF, in the absence of eGFP (because of the size limit of the cDNA insertion in the AAV vector; see Materials and Methods), randomly selected IHCs were recorded in the organ of Corti. Only one of seven IHCs did not show a significant increase in exocytosis compared with noninjected *Otof*$^{-/-}$ mice. This high rate of exocytosis rescue in AAV-*Otof*-C2-DEF-injected cochleae was consistent with the high percentage (>90%) of IHCs expressing the mini-otoferlin protein (Fig. 1*E*). The kinetics of exocytosis for *Otof*-C2-DEF-transduced IHCs were significantly higher than in *Otof*$^{-/-}$ IHCs (two-way ANOVA, $p = 6.8\ 10^{-13}$; *post hoc* Tukey's test, $p = 1.7\ 10^{-3}$; Fig. 3*C*).

Remarkably, recordings from *Otof*$^{-/-}$ IHCs of AAV-*Otof*-C2-ACEF-injected cochlea displayed a more efficient rescue of exocytosis when stimulated with brief depolarizing impulses lasting <20 ms (Fig. 3*A*,*B*). Only 1 of 10 IHCs recorded from AAV-*Otof*-C2-ACEF-injected mice did not produce a ΔC_m response different from that of *Otof*$^{-/-}$ IHCs of noninjected cochleae, again a result in good agreement with the high percentage of transduced IHCs (Fig. 1*C*,*D*). The kinetics of exocytosis for *Otof*-C2-ACEF were significantly higher than in *Otof*$^{-/-}$ IHCs (two-way ANOVA, $p = 6.8\ 10^{-13}$, $p < 10^{-4}$; Fig. 3*B*). The kinetics of exocytosis with *Otof*-C2-ACDF were also found to be significantly higher than in *Otof*$^{-/-}$ IHCs (two-way ANOVA, $p = 6.8\ 10^{-13}$, $p = 2.2\ 10^{-3}$; Fig. 3*C*).

The most common method to quantify the RRP is to fit the data with a single exponential function, with time constant (τ) giving 63.2% of the RRP value. For WT control IHCs, we found a RRP value of 19.3 ± 2.6 fF with $\tau = 29.5 \pm 6.5$ ms. In our experimental conditions, whereas the data for *Otof*-C2-EF (RRP = 5.0 ± 0.8 fF with $\tau = 15.5 \pm 7.3$ ms), *Otof*-C2-ACEF (RRP = 5.9 ± 0.3 fF with $\tau = 8.5 \pm 1.9$ ms), and *Otof*-C2-DEF (RRP = 4.5 ± 0.5 fF with $\tau = 19.0 \pm 5.2$ ms) could be fitted with a single exponential, we could not accurately fit the data for *Otof*-C2-ACDF and *Otof*$^{-/-}$ with such a function and therefore determine RRP values for these conditions. Therefore, to be able to statistically compare all mini-*Otof* conditions and controls within a single one-way ANOVA, we instead compared the initial rate of RRP exocytosis. This RRP rate was obtained for each condition by fitting the first four time points of each of the kinetics with a linear function. All mini-*Otof*s, except *Otof*-C2-ACDF, showed a significant increase in the rate of the RRP exocytosis compared with *Otof*$^{-/-}$ IHCs (Fig. 3*D*, Table 2).

The Ca^{2+} efficiency of RRP exocytosis ($\Delta C_m/Q_{Ca}$; Q_{Ca} is defined as the integral of the Ca^{2+} current) in *Otof*-C2-ACEF IHCs was also found to be similar to that in WT controls for brief depolarizations lasting up to 15 ms, with mean slopes of 2.77 ± 0.21 fF/pC and 2.09 ± 0.28 fF/pC, respectively (Fig. 3*E*; *F* test with $F = 2.18$, $p = 0.23$). These results indicate that the abridged short otoferlin, *Otof*-C2-ACEF, was able to trigger fast vesicular membrane fusion as efficiently as the native six-C2 otoferlin.

However, *Otof*$^{-/-}$ IHCs treated with the mini-*Otof*, although showing partial recovery of the RRP release, could not efficiently sustain exocytosis for voltage impulses during a train of stimulations compared with WT IHCs (Fig. 3*F*,*G*), suggesting a defect in the vesicle pool replenishment process. The Ca^{2+} efficiency of exocytosis ($\Delta C_m/Q_{Ca}$) measured for voltage steps beyond 20 ms up to 40 ms was significantly reduced from 1.69 ± 0.29 fF/pC in WT to 0.56 ± 0.14 fF/pC in *Otof*-C2-ACEF IHCs (Fig. 3*E*; *F* test with $F = 16.0$, $p = 0.0039$). The replenishment rate, calculated during a train of depolarizations, was reduced by a factor of 3 to 5 compared with WT IHCs, although it was significantly larger, except for *Otof*-C2-ACDF, than for *Otof*$^{-/-}$ IHCs from nonin-

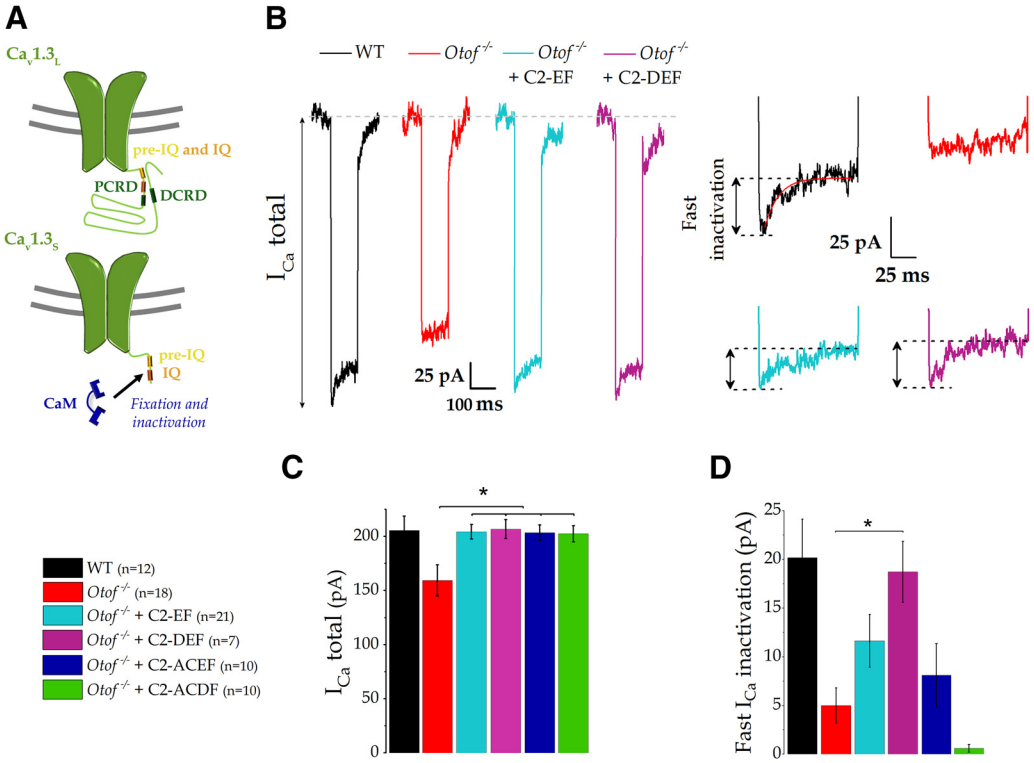

Figure 4. AAV gene transfer of mini-*Otof* restores the fast inactivating component of the Ca^{2+} current in P15–P21 *Otof*$^{-/-}$ IHCs. ***A***, IHCs are thought to express long and short C-terminal $Ca_v1.3$ isoforms (Scharinger et al., 2015, Vincent et al., 2017). Short C-terminal $Ca_v1.3$ channel isoforms are rapidly inactivated by calmodulin and are thought to carry the fast component of Ca^{2+} current inactivation (Vincent et al., 2017). C-terminal regulatory domains (PCRD and DCRD) of long $Ca_v1.3$ isoforms compete with CaM, and these channels, representing the major isoforms, do not present fast inactivation (IQ indicates the isoleucine-glutamine motif domain interacting with Ca^{2+}/CaM). ***B***, Unlike WT IHCs (black trace), IHCs lacking otoferlin (red trace) do not display Ca^{2+} current with fast inactivation (Vincent et al., 2017). ***C***, Peak I_{Ca} (I_{Ca} total) is significantly diminished in *Otof*$^{-/-}$ mice compared with WT mice, but the expression of all mini-otoferlins allows the recovery of the I_{Ca} current (one-way ANOVA; see Table 2). ***D***, Only when the mini-otoferlin C2-DEF is virally expressed in IHCs is the amplitude of the inactivating component of the Ca^{2+} current (fitted with a single exponential over the first 50 ms of the current trace) significantly recovered compared with *Otof*$^{-/-}$ (Kruskal–Wallis; see Table 2). IHCs were depolarized for 100 ms from −80 to −10 mV. *$p <$ 0.05. Error bars indicate SE.

jected mice (Fig. 3*G*). This defect in the vesicle pool resupply to the RRP, found also in the *pachanga* mouse model with a point mutation in C2-F (Pangrsic et al., 2010), explains the absence of ABR waves in these mini-*Otof*-injected mice (Fig. 2).

Mini-*Otof* constructs partially restore the fast Ca^{2+} current inactivation in *Otof*$^{-/-}$ IHCs

Cochlear IHCs have been shown to express long and short C-terminal $Ca_v1.3$ isoforms (Scharinger et al., 2015, Vincent et al., 2017). Short C-terminal $Ca_v1.3$ channel ($Ca_v1.3_S$) isoforms lacking the C-terminal modulator (Bock et al., 2011) are rapidly inactivated by calmodulin (CaM) and are thought to carry the fast component of Ca^{2+} current inactivation in IHCs (representing 15–30% of the total calcium current; Vincent et al., 2017; Fig. 4*A*). The distal and proximal C-terminal regulatory domains (DCRD and PCRD, respectively) of long $Ca_v1.3$ ($Ca_v1.3_L$) isoforms compete with CaM, and these channels do not present fast inactivation. These $Ca_v1.3_L$ isoforms likely support the major part of the Ca^{2+} current in IHCs (Fig. 4*A*; Vincent et al., 2017). Unlike WT IHCs, IHCs lacking otoferlin display Ca^{2+} currents with weak or no inactivation, suggesting that otoferlin is required for the functional expression of $Ca_v1.3_S$ isoforms in IHCs (Vincent et al., 2017; Fig. 4*B*,*4D*). WT IHCs displayed a fast inactivating component with an amplitude of 20 ± 4 pA, with τ = 20.3 ± 3.3 ms, when fitting the first 50 ms of the current trace with a single exponential function, an amplitude significantly larger than that for *Otof*$^{-/-}$ IHCs (5 ± 2 pA; Kruskal–Wallis, p = 1.5 10^{-6}; Dunn's *post hoc* test with p = 3.7 10^{-3}; with similar τ = 20.4 ± 3.5 ms). Also, the peak amplitude of the Ca^{2+} currents was smaller in P15–P21 *Otof*$^{-/-}$ IHCs compared with P15–P21 WT IHCs (Fig. 4*C*; one-way ANOVA, p = 1.3 10^{-3}; Tukey's *post hoc* test, p = 5.3 10^{-3}). Remarkably, the expression of all the mini-*Otof*s tested, even *Otof*-C2-ACDF, which poorly rescues RRP exocytosis, restored the amplitude of Ca^{2+} currents in P15–P21 *Otof*$^{-/-}$ IHCs to levels comparable to those of WT IHCs (Fig. 4*C*, Table 2). However, only *Otof*-C2-DEF restored the fast inactivating component of the Ca^{2+} current in *Otof*$^{-/-}$ IHCs (mean amplitude of 19 ± 3 pA with τ = 20.6 ± 3.2 ms) compared to *Otof*$^{-/-}$ IHCs (5 ± 2 pA with τ = 20.4 ± 3.5 ms), when IHCs were stepped from −80 to −10 mV (Table 2, Fig. 4*D*). These results are in good agreement with previous *in vitro* protein–protein interaction assays showing that otoferlin can interact through its C-terminal C2 domains, notably C2-D, with the $Ca_v1.3$ channels (Ramakrishnan et al., 2009; Hams et al., 2017). Furthermore, they confirm that otoferlin is essential for the functional expression of the fast inactivating $Ca_v1.3_S$ in IHCs (Vincent et al., 2017), likely through a functional interaction between C2-DEF and $Ca_v1.3_S$. Note that none of the combinations of the four C2 domain constructs C2-ACEF or C2-ACDF resulted in a significant recovery of the fast inactivating component of Ca^{2+} current (Fig. 4*D*). We recall that to insert the four C2 domains of the mini-*Otof* into the AAV construct, we truncated some of the inter-C2 sequence between the domains C2-A–C2-C and C2-E–C2-F for ACEF (Fig. 1*A*; Materials and Methods). A similar trun-

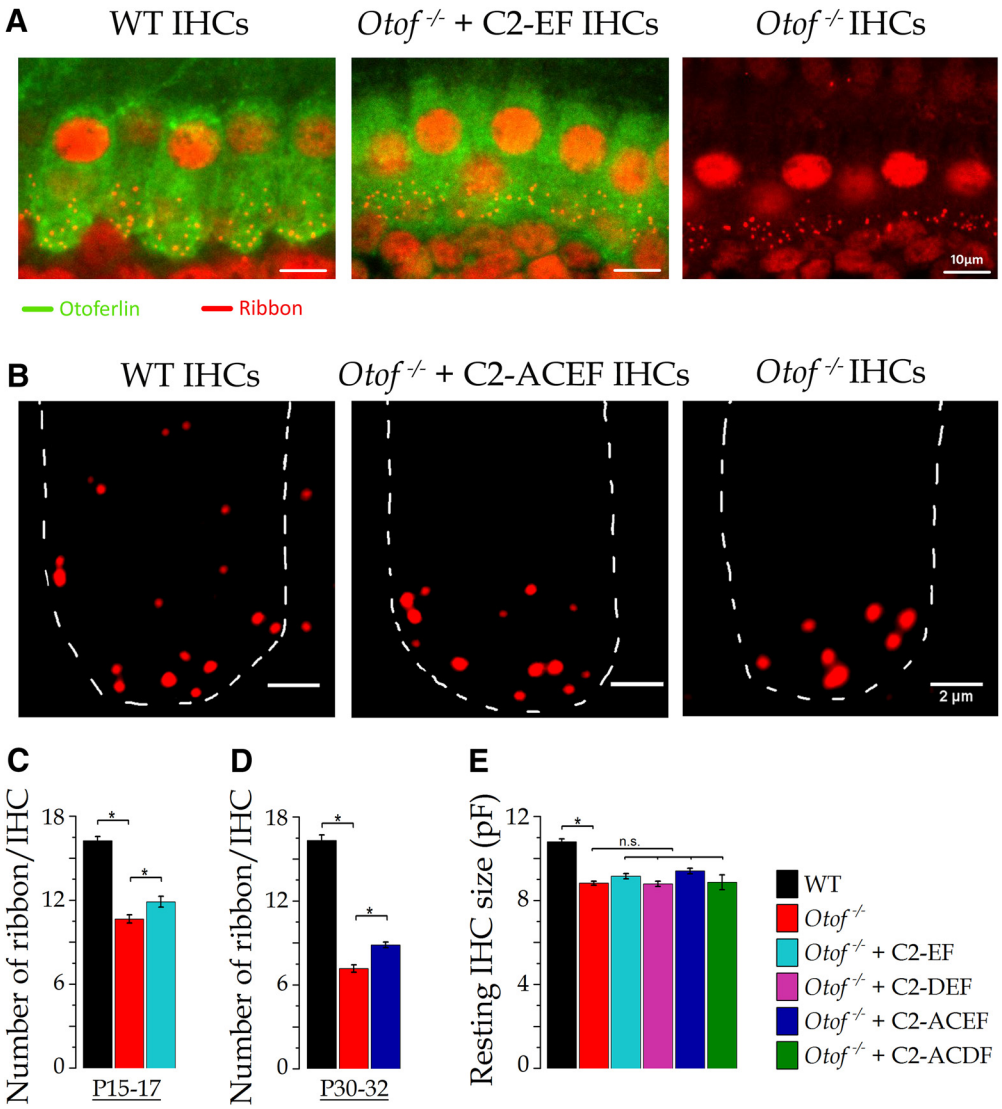

Figure 5. Mini-*Otof* constructs partially rescued the synaptic ribbon numbers the synaptic ribbon numbers in $Otof^{-/-}$ IHCs. ***A***, Using immunofluorescent confocal imaging, we quantified the number of synaptic ribbons (red dots) at P15–P17 in IHCs from WT, $Otof^{-/-}$ expressing the otoferlin C2-EF domain, and $Otof^{-/-}$ mice. The green signal indicates otoferlin expression in WT and C2-EF but not in noninjected $Otof^{-/-}$ IHCs. ***B***, Immunolabeling examples of synaptic ribbons (at larger magnification; without otoferlin immunolabeling) in P30–P32 IHCs from a WT (control) mouse, an $Otof^{-/-}$ mouse injected with C2-ACEF, and a noninjected $Otof^{-/-}$ mouse. The dashed white line delineates the cell contour at the basal synaptic area of one IHC for each category. ***C***, Comparative ribbon histogram at P15–P17 for C2-EF: IHCs of $Otof^{-/-}$ mice displayed a largely reduced number of ribbons (10.7 ± 0.3; $n = 70$ IHCs; 3 mice) compared with WT mice (16.2 ± 0.3, $n = 40$ IHCs, one-way ANOVA, $p < 10^{-4}$). The *Otof*-C2-EF expression in $Otof^{-/-}$ IHCs had a significantly larger number of ribbons per cell (11.9 ± 0.4; $n = 43$ IHCs) compared with control, noninjected $Otof^{-/-}$ mice (10.7 ± 0.3; $n = 70$ IHCs; one-way ANOVA, $p = 0.022$). ***D***, Comparative histograms at P30–P32 for C2-ACEF: IHCs of C2-ACEF-injected mice also displayed a significant preservation of synaptic ribbons (8.8 ± 0.2, $n = 31$ IHCs) compared with control, untreated $Otof^{-/-}$ mice (7.1 ± 0.3; $n = 56$ IHCs; Kruskal–Wallis, $p = 1.8\ 10^{-3}$). ***E***, The resting size of $Otof^{-/-}$ IHCs, measured in whole-cell recordings at −70 mV, was diminished compared to the WT IHC resting size (8.8 ± 0.09 pF, $n = 53$; 10.79 ± 0.14 pF, $n = 43$ respectively; one-way ANOVA, $p < 10^{-4}$). None of the mini-*Otof*s significantly restored the resting size of IHCs. The asterisks indicate significantly different with $p < 0.05$ (for each compared to $Otof^{-/-}$ mice, one-way ANOVA). Error bars indicate SE.

cation was done for ACDF. It is therefore possible that these inter-C2 sequences are important for Ca^{2+} current inactivation while leaving intact the membrane expression level of the Ca^{2+} channels.

Mini-*Otof* constructs partially restore the number of synaptic ribbons in $Otof^{-/-}$ IHCs

As described previously by Vincent et al. (2017), we found that IHCs from $Otof^{-/-}$ mice displayed a significantly lower number of synaptic ribbons at P15–P17 compared to WT IHCs (Fig. 5*A*,*C*): 10.7 ± 0.3 ribbons per cell ($n = 70$ $Otof^{-/-}$ IHCs from three mice) and 16.2 ± 0.3 ($n = 40$ WT IHCs from three mice; one-way ANOVA, $p < 10^{-4}$; Tukey's *post hoc* test, $p < 10^{-4}$), respectively. This comparative quantification of the ribbon numbers was done in the same cochlear area where the patch-clamp recordings were performed (20–40% normalized distance from the cochlear apex corresponding to encoding frequencies between 8 and 16 kHz). Note that the mean number of ribbons per WT IHC is consistent with previous findings (Meyer et al., 2009; Vincent et al., 2014). We found that the viral expression of *Otof*-C2-EF in P15–P17 $Otof^{-/-}$ IHCs leads to a significant increase in the number of ribbons per IHC compared with noninjected and sham $Otof^{-/-}$ IHCs: 11.9 ± 0.4 ribbons per IHC ($n = 43$ IHCs from three mice; one-way ANOVA, $p = 0.022$; Fig. 5*C*). The number of synaptic ribbons per IHC in control untreated $Otof^{-/-}$ mice continued to decrease to 7.1 ± 0.3 ribbons ($n = 56$ IHCs) at P30–P32 compared to P15–P17 (unpaired *t* test, $p < 10^{-4}$; Fig. 5*C*,*D*). Again, cochlear injection of C2-ACEF in

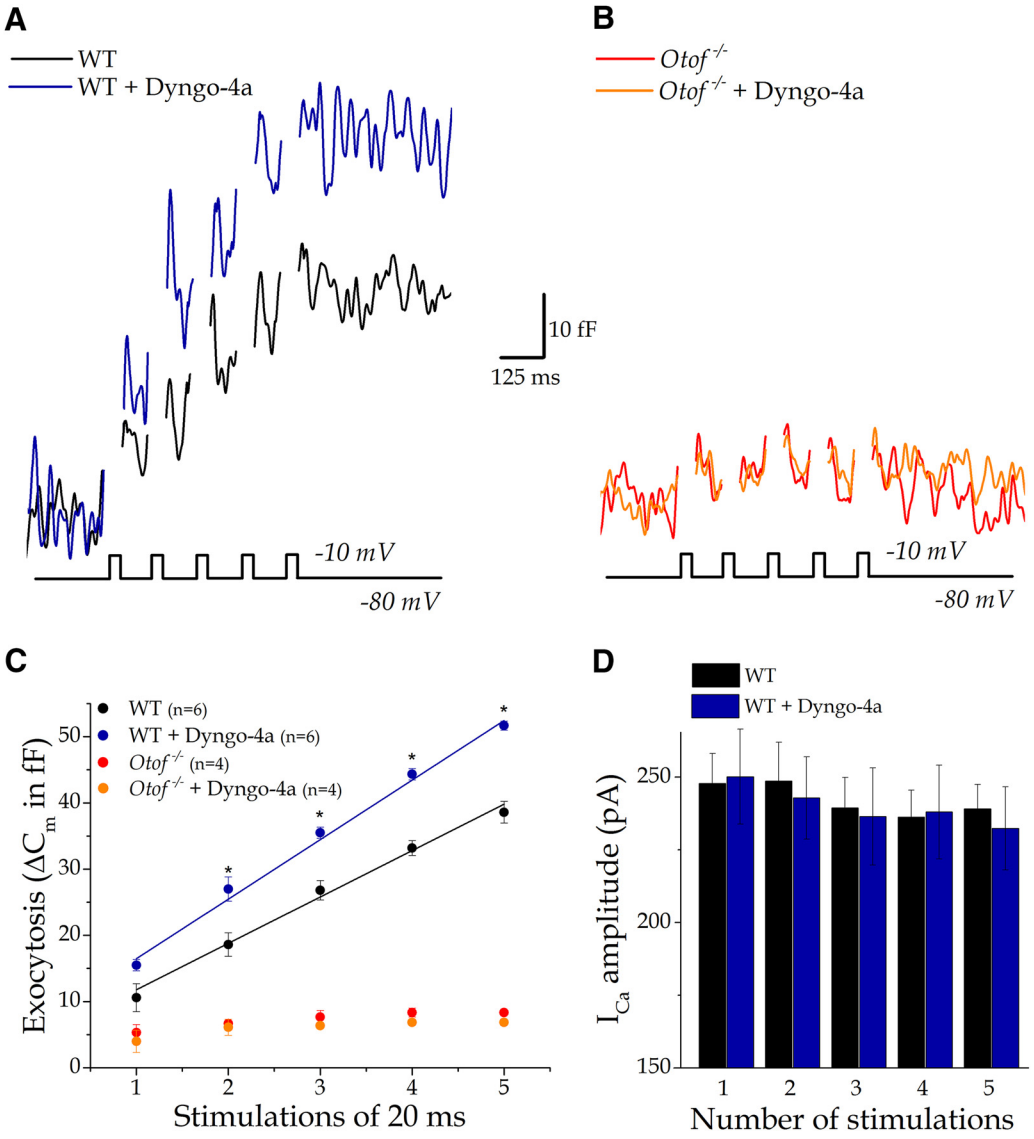

Figure 6. The effect of a dynamin inhibitor on RRP exocytosis. ***A***, ***B***, We tested the effect of 30 μM Dyngo-4a (dynamin inhibitor) on the ΔC_m response in P15–P21 IHCs from WT (***A***) and in *Otof*$^{-/-}$ mice (***B***) by applying five consecutive brief 20 ms depolarizing pulses. ***C***, The presence of Dyngo-4a increased the net ΔC_m responses in WT IHCs by blocking endocytosis. *$p < 0.05$ (unpaired *t* test). Dyngo-4a did not affect the ΔC_m responses in *Otof*$^{-/-}$ IHCs. ***D***, The increase in ΔC_m responses in WT IHCs was not the result of augmented Ca^{2+} currents since similar amplitudes were found in the presence or absence of the endocytotic inhibitor. Error bars indicate SE.

Otof$^{-/-}$ mice led to a significant preservation of about two ribbons per IHC at P30–P32 compared to untreated control *Otof*$^{-/-}$ mice (8.8 ± 0.2; $n = 31$ IHCs; Kruskal–Wallis, $p = 6.7\ 10^{-9}$; Dunn's post-test, $p = 1.8\ 10^{-3}$; Fig. 5*D*). The incomplete preservation of the ribbons with C2-EF and C2-ACEF was in line with the partial restoration of the RRP responses (Fig. 3*A*,*B*).

Also, as described previously (Vincent et al., 2014, 2015, 2017), we found that the resting whole-cell membrane capacitance of IHCs from *Otof*$^{-/-}$ mice, measured at $V_H = -70$ mV, was significantly reduced compared with WT IHCs: 8.8 ± 0.09 pF ($n = 53$) and 10.79 ± 0.14 pF ($n = 43$; one-way ANOVA, $p = 2.9\ 10^{-7}$; Tukey's *post hoc* test, $p = 8.7\ 10^{-7}$), respectively (Fig. 5*E*). This reduction in surface membrane area of IHCs lacking otoferlin can be explained by a reduced resting vesicular exocytosis and a sustained otoferlin-independent slow endocytosis (Vincent et al., 2014). The viral expression of all mini-*Otof* in *Otof*$^{-/-}$ IHCs, did not produced a significant change in the resting IHC membrane capacitance compared with *Otof*$^{-/-}$ IHCs (one-way ANOVA; Tukey's *post hoc* test, $p > 0.05$; Fig. 5*E*).

Mini-*Otof* constructs reveal ultrafast endocytosis in *Otof*$^{-/-}$ IHCs

Dyngo-4a, by blocking endocytosis, increases exocytosis evoked by voltage activation of Ca^{2+} channels

Dyngo-4a is a highly potent inhibitor of dynamin, a GTP binding protein essential for ultrafast endocytosis (Watanabe et al., 2013a, b). Dynamin is thought to polymerize around the neck of the synaptic vesicles that are fused with the plasma membrane, leading to a fast membrane fission and pinching off of the vesicle from the plasma membrane active zone. Both dynamin 1 and 3 are expressed in IHCs (Neef et al., 2014; Shen et al., 2015). We first tested the effect of external application of 30 μM Dyngo-4a on the mobilization of the RRP evoked by five consecutive brief 20 ms depolarizing pulses, with an interpulse interval of 100 ms, in P15–P21 WT IHCs (Fig. 6*A*). Remarkably, the dynamin inhibitor largely increased the RRP responses (Fig. 6*A*,*C*). The increase in ΔC_m responses was not the result of increased Ca^{2+} currents since similar amplitudes were found in the presence or absence of the endocytotic inhibitor (Fig. 6*D*). If we consider that the ΔC_m

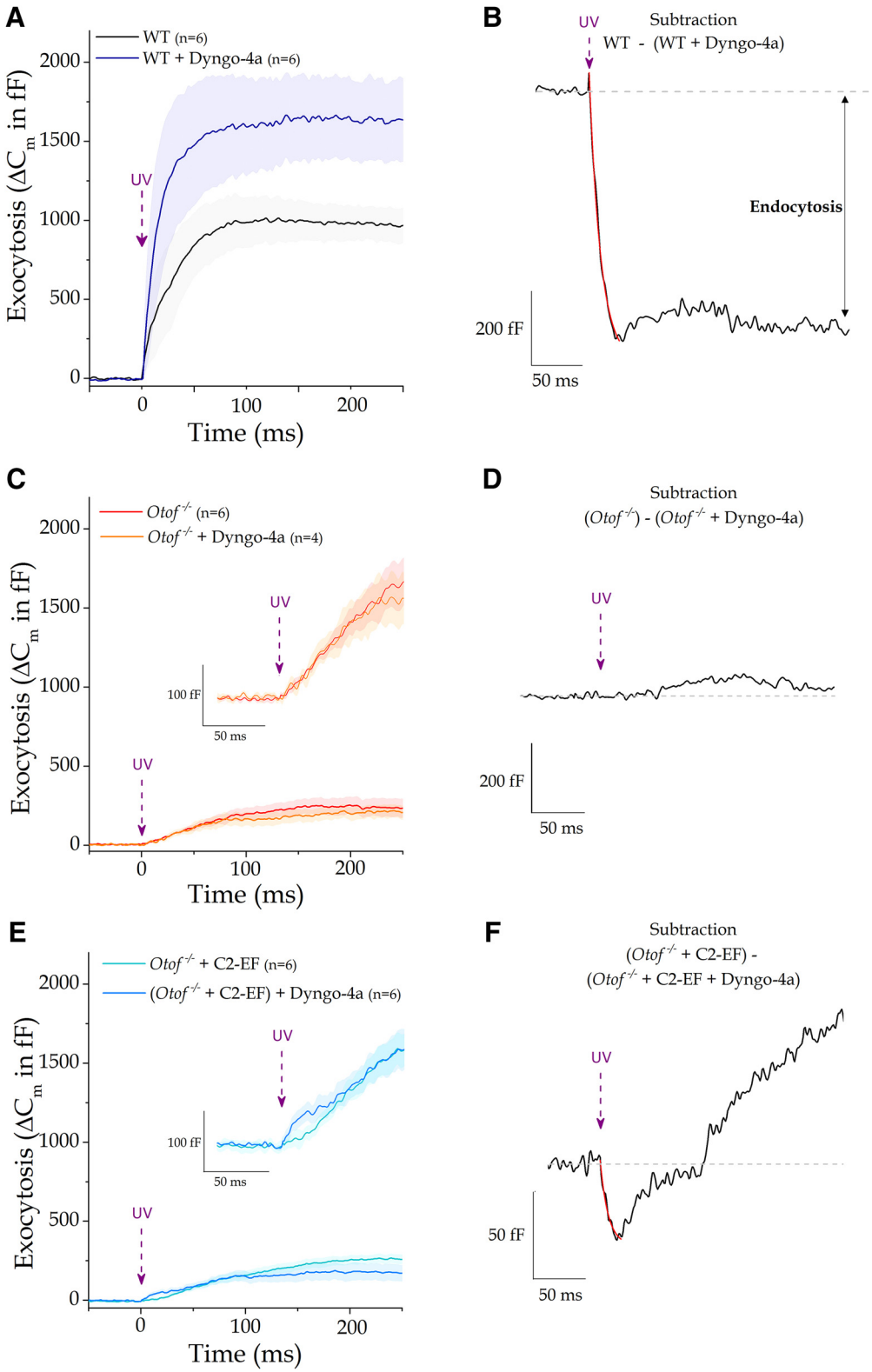

Figure 7. Dyngo-4a effects on exocytosis evoked by intracellular Ca^{2+} uncaging ***A***, We tested the effect of Dyngo-4a on the exocytotic responses evoked by intracellular Ca^{2+} uncaging in WT P15–P21 IHCs. In the presence of Dyngo-4a (dark blue), we observed an increased in the kinetics and amplitude of the ΔC_m responses. ***B***, The subtraction of the ΔC_m responses reveals the presence of an ultrafast endocytosis (best fitted with a single exponential with $\tau = 10.9 \pm 0.5$ ms). ***C***, ***D***, The presence of Dyngo-4a has no effect on exocytosis in *Otof*$^{-/-}$ IHCs. ***E***, When Dyngo-4a was added to *Otof*-C2-EF IHCs, the initial rate of the exocytotic response was transiently increased. ***F***, The subtraction of the ΔC_m responses revealed a transient ultrafast endocytosis ($\tau = 7.6 \pm 1.0$ ms) followed by exocytosis.

Table 3. Summary of ultrafast endocytosis

Subtraction	Amplitude (fF)	Time constant (ms)	Mean maximal rate (dC_m/dt, in fF/ms)
Fig. 7*B*			
WT ($n = 6$) − [WT ($n = 6$) + Dyngo-4a]	737.1	10.9 ± 0.5	70.7
Fig. 7*D*			
Otof$^{-/-}$ ($n = 6$) − [*Otof*$^{-/-}$ ($n = 4$) + Dyngo-4a]	—	—	—
Fig. 7*F*			
C2-EF ($n = 6$) − [C2-EF ($n = 6$) + Dyngo-4a]	44.7	7.6 ± 1.0	7.9
Fig. 8*D*			
[*Otof*$^{-/-}$ ($n = 6$) + C2-EF] − *Otof*$^{-/-}$ ($n = 7$)	38.2	10.7 ± 1.3	5.0
Fig. 8*B*			
[*Otof*$^{-/-}$ ($n = 11$) + C2-DEF] − *Otof*$^{-/-}$ ($n = 7$)	35.8	16.0 ± 4.7	7.0
Fig. 8*F*			
[*Otof*$^{-/-}$ ($n = 6$) + C2-ACEF] − *Otof*$^{-/-}$ ($n = 6$) (exocytosis)	57.3	5.2 ± 2.5	6.9
[*Otof*$^{-/-}$ ($n = 6$) + C2-ACEF] − *Otof*$^{-/-}$ ($n = 6$) (endocytosis)	65.7	87.2 ± 12.9	0.8
Data not shown			
[*Otof*$^{-/-}$ ($n = 8$) + C2-ACDF] − *Otof*$^{-/-}$ ($n = 7$)	32.7	21.5 ± 10.7	1.6

A dash indicates a nonmeasurable endocytosis.

responses result from the net difference between exocytosis and endocytosis, the increasing effect of Dyngo-4a on the ΔC_m response suggested that a 20 ms time scale endocytosis in IHCs was blocked, a time scale in the range of the ultrafast endocytosis described in central synapses (Watanabe et al., 2013b). Notably, application of Dyngo-4a had no effect on the ΔC_m responses recorded in *Otof*$^{-/-}$ IHCs, suggesting that the small residual otoferlin-independent exocytosis was not large enough to trigger measurable ultrafast endocytosis (Fig. 6*B*,*C*). Alternatively, this result suggested that otoferlin is required for ultrafast endocytosis.

Dyngo-4a increases the ΔC_m *responses triggered upon intracellular* Ca^{2+} *uncaging*

The effect of Dyngo-4a was also tested on ΔC_m responses evoked during intracellular Ca^{2+} uncaging experiments (Fig. 7). In these conditions, in WT IHCs, we observed a significant increase in the rate of the ΔC_m responses, calculated as the first derivative at each point of the ΔC_m response curve, in the presence of Dyngo-4a responses (maximal dC_m/dt of 42.8 ± 2.2 fF/ms and 88.4 ± 3.9 fF/ms, respectively, without and with Dyngo-4a; unpaired *t* test, $p = 0.019$). Also, the maximum amplitude was significantly larger in the presence of Dyngo-4a (from 1293 ± 26 fF to 1813 ± 57 fF; unpaired *t* test, $p = 0.027$; Fig. 7*A*), again suggesting that ultrafast endocytosis occurs concomitantly with exocytosis. Subtracting the ΔC_m responses produced by Ca^{2+} uncaging in the presence of Dyngo-4a from those obtained in the absence of Dyngo-4a indicated an ultrafast endocytosis with a time constant of $\tau = 10.9 \pm 0.5$ ms, a maximal amplitude of 737.1 ± 24.9 fF, and a maximal rate (dC_m/dt) of 70.7 fF/ms (Fig. 7*B*, Table 3). Of note, Dyngo-4a had no significant effect on the rate of ΔC_m responses evoked by Ca^{2+} uncaging in noninjected *Otof*$^{-/-}$ IHCs (maximal rates of 2.0 ± 0.1 fF/ms and 2.2 ± 0.1 fF/ms, with and without Dyngo-4a, respectively; unpaired *t* test, $p = 0.74$), again indicating that the rate of exocytosis in the absence of otoferlin is too slow to trigger ultrafast endocytosis and/or that otoferlin is required for endocytosis (Fig. 7*C*,*D*).

We then tested the effects of Dyngo-4a on Ca^{2+} uncaging-evoked exocytosis in *Otof*$^{-/-}$ IHCs expressing *Otof*-C2-EF. Remarkably, the presence of Dyngo-4a significantly increased the initial mean rate of exocytosis during the first 20 ms after the UV flash (from 0.9 ± 0.1 fF/ms without Dyngo-4a and 2.8 ± 0.1 fF/ms with Dyngo-4a; unpaired *t* test, $p = 0.02$; Fig. 7*E*). Subtracting the traces in the presence of Dyngo-4a from those in its absence again indicated a transient fast initial decrease in ΔC_m, that is, an ultrafast endocytosis with a maximal amplitude of 44.7 ± 4.3 fF, a time constant of 7.6 ± 1.0 ms, and a maximal rate of 7.9 fF/ms (Fig. 7*F*, Table 3). Surprisingly, the endocytotic response was transient and followed by an increase in membrane capacitance (Fig. 7*F*). This was likely due to the fact that in the presence of Dyngo-4a, the exocytotic response depressed more rapidly with time than that for the untreated control *Otof*$^{-/-}$ IHCs (Fig. 7*E*). This suggests that vesicle endocytosis could participate in local fast recycling of synaptic vesicles, and this process contributes to sustain release.

It is unlikely that the IHC capacitance responses measured during Ca^{2+} uncaging result or is contaminated by thermal excitation of the mechanoelectrical transduction apparatus and depolarization (Azimzadeh et al., 2018). In this later study, the power density of the UV laser used to generate thermal effect in hair cells is extremely high, more than three orders of magnitude larger than our UV power density generated with our UV LED. Our UV LED flash produced no significant thermal effect to stimulate the hair cells. Strong arguments for this assumption come from the absence of sustained repetitive C_m responses once intracellular DM-Nitrophen is photolyzed, when applying repetitive consecutive UV flashes, or the absence of C_m response when flashing the IHCs with the UV LED in the absence of intracellular DM-Nitrophen (our unpublished data). Furthermore, recordings in whole-cell voltage-clamp conditions should minimize UV-induced membrane depolarization in our study.

Why was endocytosis, unmasked by Dyngo-4a, first transiently observed during Ca^{2+} uncaging in *Otof*$^{-/-}$ IHCs *Otof*-C2-EF? One possible explanation is that endocytosis, a Ca^{2+}-dependent process (Yamashita et al., 2010), is more Ca^{2+} sensitive compared with exocytosis but is inhibited at high Ca^{2+} concentrations at which exocytosis is still activated, as proposed previously at synaptic terminals of bipolar neurons by von Gersdorff and Matthews (1994a,b). It is worth noting that our UV-LED-Ca^{2+} uncaging system was measured to rise the concentration of intracellular Ca^{2+} in IHCs to 20 μM within 15–20 ms (Michalski et al., 2017).

The amplitude of endocytosis, revealed by Ca^{2+} uncaging and the effect of Dyngo-4a, was much smaller in *Otof*$^{-/-}$ IHCs expressing the mini-*Otof* constructs C2-EF compared with WT IHCs. However, the endocytotic time constant was similarly ultrafast, respectively 7.6 and 10.9 ms, suggesting that this Dyngo-4a-sensitive process was similar. The difference in rate and amplitude could be explained by the fact that the mini-otoferlin C2-EF incompletely restores the rate of vesicle fusion and/or, more importantly, the vesicle replenishment, as indicated in Figure 3.

*Mini-*Otof *constructs reveal ultrafast endocytosis during intracellular* Ca^{2+} *uncaging*

When compared with a new set of noninjected *Otof*$^{-/-}$ IHCs, uncaging intracellular Ca^{2+} in P15–P21 IHCs from mouse injected with AAV8-C2-DEF displayed an initial decrease in the

rate of the ΔC_m responses from 1.83 ± 0.01 fF/ms to 1.10 ± 0.01 fF/ms (unpaired *t* test, $p = 0.036$, Fig. 8*A*). The subtraction of the traces gave a mean ultrafast endocytosis amplitude of 35.8 ± 4.6 fF, a time constant of 16.0 ± 4.7 ms and maximal rate dC_m/dt of 7.0 fF/ms (Fig. 8*B*, Table 3). Similar ultrafast endocytosis was obtained with *Otof*-C2-EF (Fig. 8*C–D*, Table 3) and *Otof*-C2-ACDF (curve not shown; Table 3). The initial rates of endocytosis produced by *Otof*-C2-DEF, *Otof*-C2-EF, and *Otof*-C2-ACDF may have been underestimated because the change in membrane capacitance upon Ca^{2+} uncaging likely results at each point of the curve from the balance of exocytosis and endocytosis and we cannot rule out that these two events occur concomitantly. Remarkably, the initial endocytosis was rapidly followed by exocytosis in IHCs from *Otof*-C2-DEF and *Otof*-C2-EF injected mice but not in *Otof*-C2-ACDF (data not shown), in agreement with their respective efficiency in restoring exocytosis when voltage-stepping the cells (Fig. 3*A–C*). During the voltage-activation of Ca^{2+} currents in Figure 3*A–C*, it is likely that we missed the initial transient ultrafast endocytosis because of the recording blind window inherent to the single sine-wave C_m measurement technique during the Ca^{2+} current activation.

Uncaging intracellular Ca^{2+} in IHCs from mouse injected with AAV8-C2-ACEF showed an initial increase of the exocytotic response from 2.31 ± 0.03 fF/ms to 3.90 ± 0.14 fF/ms (Fig. 8*E*; unpaired *t* test, $p = 0.022$). Subtracting the ΔC_m responses of *Otof*-C2-ACEF-injected IHCs from noninjected $Otof^{-/-}$ IHCs (new set of $Otof^{-/-}$ IHCs recorded simultaneously to *Otof*-C2-ACEF-injected IHCs) indicated first a transient exocytosis with mean amplitude of 57.3 ± 6.4 fF, a time constant of 5.2 ± 2.5 ms and maximal rate dC_m/dt of 6.9 fF/ms (Fig. 8*F*, Table 3). This initial exocytotic response was transient and followed by a fast C_m decrease likely reflecting ultrafast endocytosis with a mean amplitude of 65.7 ± 4.1 fF, a time constant of 87.2 ± 12.9 ms and maximal rate dC_m/dt of 0.8 fF/ms. Why Ca^{2+} uncaging in $Otof^{-/-}$ IHCs expressing *Otof*-C2-ACEF first produced a transient fast exocytosis? This is possibly due to the higher efficiency of Otof-C2-ACEF to restore RRP exocytosis compared to *Otof*-C2-EF or *Otof*-C2-DEF (Fig. 3). Then, endocytosis in *Otof*-C2-ACEF IHCs was only revealed secondary to exocytosis when the vesicular RRP pool was exhausted because of the absence of an efficient vesicle replenishment. Alternatively *Otof*-C2-ACEF, while being highly Ca^{2+} efficient for exocytosis could be much less effective for endocytosis as indicated by its lower rate and time constant compared to *Otof*-C2-EF.

Discussion

Restoration of RRP exocytosis with mini-otoferlins

We showed that expression of the mini-otoferlins *Otof*-C2-EF, *Otof*-C2-DEF, and *Otof*-C2-ACEF can partially restore RRP exocytosis in $Otof^{-/-}$ IHCs. *Otof*-C2-ACEF was the most efficient, with restoration of exocytosis to levels similar to that for WT mice for stimulations <15 ms (Fig. 3*B*). C2-EF and C2-DEF constructs also restored exocytosis but only partially, up to 40% of the WT level. Interestingly, *Otof*-C2-ACDF was the less efficient mini-*Otof* and therefore revealed the importance of C2-E domain, or its association with C2-F domain at the C-terminal region of otoferlin. The C2-E domain has been shown to potentially bind to the t-SNARE protein syntaxin 1A *in vitro* (Ramakrishnan et al., 2009), a protein that is expressed in IHCs (Safieddine and Wenthold, 1999) and is generally implicated in the docking of synaptic vesicles with the presynaptic plasma membrane. The importance of the C2-F domain of otoferlin has been emphasized in the *pachanga* mouse model bearing a substitution point mutation in this domain (Pangrsic et al., 2010). In *pachanga* mice, IHCs have normal initial vesicle fusion of docked/primed vesicles but a strong defect in vesicle recruitment at the active zone. The C2-F domain can interact *in vitro* with both t-SNARE proteins (syntaxin-1A and SNAP-25) and phosphatidylinositol 4,5-bisphosphate (PIP_2) at the plasma membrane (Roux et al., 2006; Ramakrishnan et al., 2009; Padmanarayana et al., 2014; Fig. 9), similarly to the C2-B domain of synaptotagmin (Wang et al., 2016). We propose that the tandem C2-EF domain of otoferlin is at least necessary for vesicle fusion at the active zone of IHCs, presumably by interacting with the vesicle-attached t-SNARE proteins and the plasma membrane. Notably, truncated forms of otoferlin retaining the C-terminal C2-F domain were also shown to rescue the otoferlin knock-out phenotype in zebrafish (Chatterjee et al., 2015).

Interestingly, the C2-EF domain of another Ferlin-like C2-domain protein, dysferlin, is considered essential for Ca^{2+}-triggered vesicle–plasma membrane fusion in skeletal muscle cells and cardiomyocytes (Lek et al., 2012). A "mini-dysferlin," constituted by C2-EF domains and the C-terminal transmembrane domain, can be produced by intracellular calpain-1 digestion. This release of C2-EF was found to recruit vesicles to the sites of membrane injury faster than the long native form (Lek et al., 2013). A calpain-1 cleavage was also found in otoferlin, forming a possible mini-otoferlin with C2-EF and transmembrane (TM) domains (Redpath et al., 2014). Previous studies hypothesized that C-terminal dual-C2 domains (synaptotagmin-like modules) released through enzymatic cleavage of ferlin proteins have a specialized vesicle-fusion modality (Redpath et al., 2014). However, our observation that the tandem C2-EF domain of otoferlin only poorly restored RRP exocytosis suggests that this mini-otoferlin does not have a crucial function in IHCs.

Remarkably, addition of C2-A and C2-C domains to the *Otof*-C2-EF construct led to a more efficient recovery of RRP exocytosis in $Otof^{-/-}$ IHCs. These C2 domains can also potentially interact with syntaxin 1A, SNAP-25, PIP_2, and the L-type voltage-gated Ca^{2+} $Ca_v1.3$ channels (Ramakrishnan et al., 2009; Padmanarayana et al., 2014). Addition of C2-A and C2-C to C2-EF could therefore allow increased synaptic protein interactions such as a multiple binding to SNARE proteins simultaneously (Hams et al., 2017). Furthermore, C2-A and C2-C domains associated to C2-EF, forming a longer construct, could also facilitate protein folding and self C2–C2 interactions (Fig. 9). Indeed, the *Otof*-C2-ACEF could more easily form a folding tertiary structure "closed" at low Ca^{2+} concentrations that could "open" as Ca^{2+} increases to promote vesicle fusion, this model being proposed for the native otoferlin by Ramakrishnan et al. (2014). Note that open and closed states of C2-A and C2-B domains have also been proposed for synaptotagmins (Fuson et al., 2007; Evans et al., 2016). We propose that the C2-ACEF domains of otoferlin are necessary and sufficient to promote efficient Ca^{2+}-evoked vesicle fusion in IHCs.

Surprisingly, the *Otof*-C2-ACEF construct failed to restore hearing in mice lacking otoferlin, although partially rescuing RRP exocytosis. The lack of hearing restoration could be easily explained at the IHC level by the absence of efficient vesicle recruitment to the RRP vesicle component, as similar defects were also found in *pachanga* mice (Pangrsic et al., 2010). Our study confirms that the full length of otoferlin is required for efficient Ca^{2+}-dependent recruitment of the synaptic vesicles to the active zone. Full-length otoferlin, by promoting additional C2–C2 interactions, could promote the formation of long tethers holding

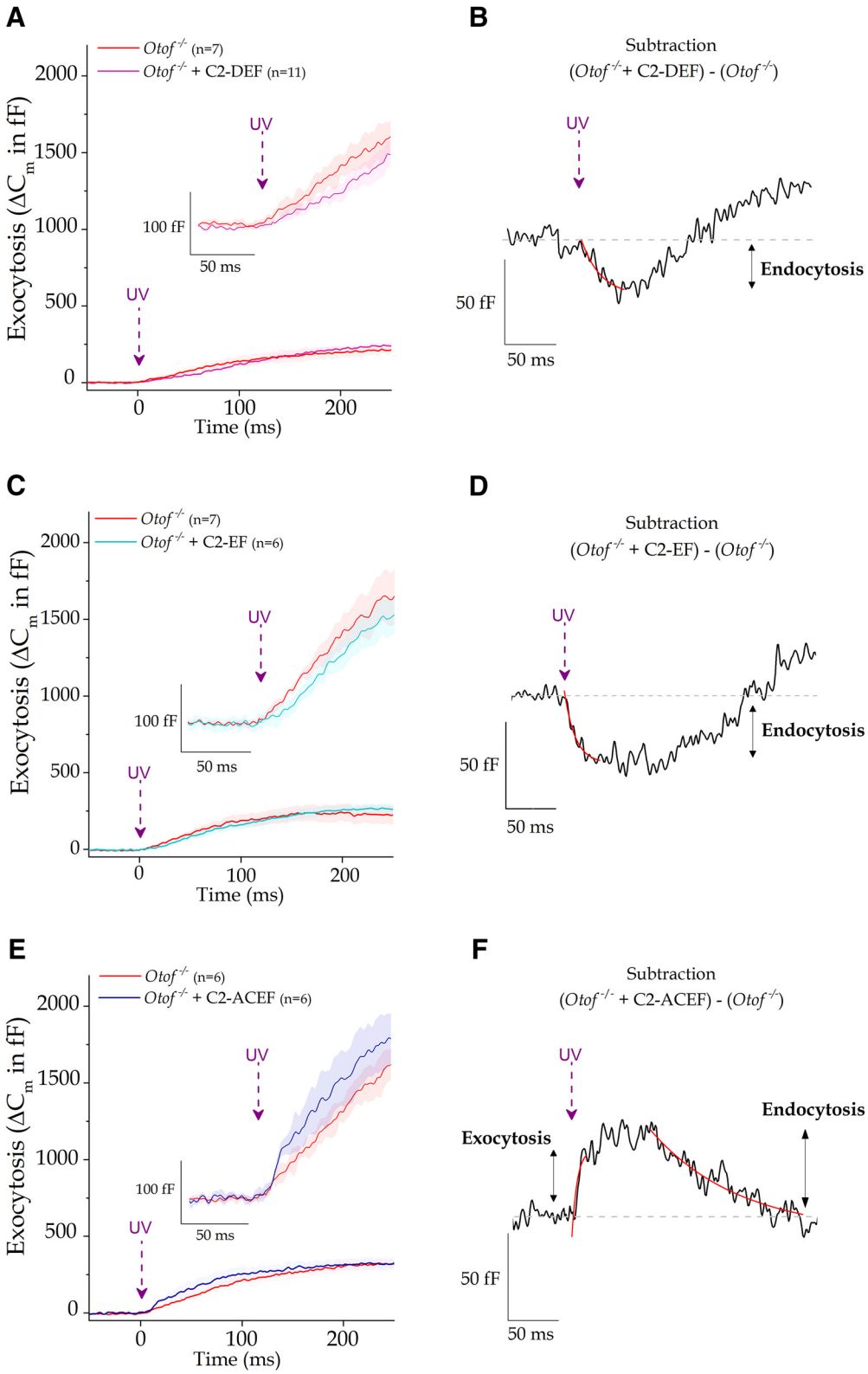

Figure 8. AAV gene transfer of mini-otoferlins revealed otoferlin-dependent ultrafast endocytosis in IHCs. ***A***, Uncaging intracellular Ca^{2+} in P15–P21 IHCs from a mouse injected with AAV8-*Otof*-C2-DEF (purple trace) displayed an initial drop in their ΔC_m responses compared with noninjected $Otof^{-/-}$ IHCs (red trace). ***B***, Subtracting the ΔC_m responses of C2-DEF-injected IHCs from those of the noninjected $Otof^{-/-}$ IHCs indicated a transient ultrafast endocytosis that could be fitted with a single exponential with $\tau = 16.0 \pm 4.7$ ms. This transient endocytosis was followed by exocytosis. ***C***, ***D***, C2-EF injection (***C***, light blue trace) also showed a transient initial ultrafast endocytosis ($\tau = 10.7 \pm 1.3$ ms). ***E***, IHCs from a mouse injected with AAV8-*Otof*-C2-ACEF (dark blue trace) showed an initial transient increase of the exocytotic response that was followed by a rapid endocytosis compared with noninjected $Otof^{-/-}$ IHCs (red trace). Note that the insets in ***A***, ***C***, ***E*** expand the Y axis of the Cm responses to see more details at the onset. ***F***, The subtraction of the ΔC_m responses (black trace) indicated a transient exocytosis ($\tau = 5.2 \pm 2.5$ ms) followed by a fast endocytotic response ($\tau = 87.2 \pm 12.9$ ms). Note that for each condition, new $Otof^{-/-}$ IHCs were simultaneously recorded in the same set of experiments. For each condition, traces are means from n IHCs, indicated in brackets in ***A***, ***C***, ***E***.

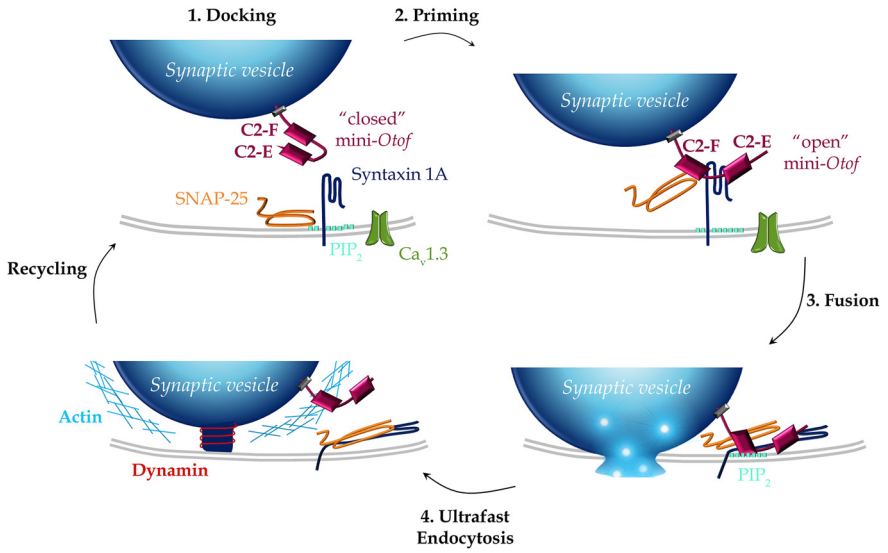

Figure 9. Schematic model for the engagement of the mini-otoferlin C2-EF in the synaptic vesicle cycle (exocytosis and endocytosis) at the IHC active zone. ***1***, Docking. The mini-*Otof* C2-EF, attached by its C-terminal transmembrane domain to the glutamatergic docked vesicles, is not yet engaged in direct interactions with the t-SNAREs (syntaxin 1A and SNAP-25) and the phospholipids PIP_2 at the plasma membrane. At low intracellular Ca^{2+} concentration, when nearby Ca^{2+} channels are not voltage activated, the mini-otoferlin is folded, and its C2-E and C2-F domains interact with each other. ***2***, Priming. During voltage activation of the Ca^{2+} channels, $[Ca^{2+}]_i$ increases and vesicles undergo a priming reaction where mini-*Otof* conformation shift from "closed" to "open" and interact with t-SNARE, forming a complex. Syntaxin 1A has been proposed to interact with C2-E and C2-F domains and SNAP-25 only with C2-F (Ramakrishnan et al., 2014). This step of the vesicle cycle is poorly restored by *Otof*-C2-EF, *Otof*-C2-DEF, *Otof*-C2-ACEF, and *Otof*-C2-ACDF (recruitment, Fig. 3*G*), explaining the absence of hearing restoration (Fig. 2). The molecular interactions of the mini-*Otof* complex with the $Ca_v1.3$ channels are not represented. ***3***, Fusion. When Ca^{2+} ions bind to the C2 domains of mini-*Otof*, the synaptic vesicle membrane and the plasma membrane are forced into close proximity by the SNARE complex, triggering partial insertion of the C2-F domain into PIP_2 and resulting in vesicle fusion. This step of vesicle fusion is partially restored by *Otof*-C2-EF, *Otof*-C2-DEF, and *Otof*-C2-ACEF. ***4***, Ultrafast vesicle endocytosis. This is mediated by dynamin, which pinches off the vesicular membrane with the help of filamentous F-actin for initializing the membrane curvature. This ultrafast endocytosis was efficiently observed with *Otof*-C2-EF, *Otof*-C2-DEF, *Otof*-C2-ACEF, and *Otof*-C2-ACDF that could interact with the dynamin process.

and priming the synaptic vesicles at the IHC active zones, a crucial structure for vesicle replenishment (Vogl et al., 2016).

Another unexpected result was that the C2-DEF mini-otoferlin did not produce a better exocytosis restoration compared with C2-EF. Notably, this C2-DEF construct, although lacking the FerA domain, closely corresponds to the short cDNA isoform found in humans but not in mice (Yasunaga et al., 2000). Therefore, our study suggests either that the short human-like otoferlin isoform does not function as an efficient Ca^{2+} sensor for exocytosis in mouse IHCs or that the FerA domain, a four helix bundle that can bind to lipids in a Ca^{2+}-dependent manner (Harsini et al., 2018), missing in our C2-DEF construct, is essential for an efficient fast vesicular fusion.

Otoferlin and Ca^{2+} channel interaction

At the IHC active zone, the $Ca_v1.3$ L-type Ca^{2+} channels, governing Ca^{2+}-triggered synaptic exocytosis in IHCs, are thought to be expressed as long and short C-terminal isoforms (Scharinger et al., 2015; Vincent et al., 2017). The short isoforms ($Ca_v1.3_S$), with fast inactivation, are essential to drive the RRP exocytosis in IHCs, whereas the long isoforms ($Ca_v1.3_L$) with slow inactivation regulate vesicle recruitment (Vincent et al., 2017). Notably, $Ca_v1.3_S$ isoforms, but not $Ca_v1.3_L$ isoforms, associate in functional cooperative clusters of two or more channels, to facilitate Ca^{2+} currents in hippocampal neurons (Moreno et al., 2016). Similarly, $Ca_v1.3_S$ could aggregate in cooperative clusters to potentiate Ca^{2+} influx at the active zone of IHCs.

The absence of otoferlin in IHCs is associated with a lack of the fast inactivating component of the Ca^{2+} currents and a decreased expression of $Ca_v1.3_S$ (Vincent et al., 2017), suggesting a functional interaction between otoferlin and $Ca_v1.3_S$ channels at the IHC synapses. Direct interactions between the II–III cytoplasmic loop of $Ca_v1.3$ and otoferlin, via the C2-D or C2-ABDF domains of otoferlin, have been suggested (Ramakrishnan et al., 2009; Hams et al., 2017). Thus, the restoration of the fast inactivating component of the Ca^{2+} currents in *Otof*$^{-/-}$ IHCs with *Otof*-C2-DEF is in agreement with the literature and confirms that the C-terminal C2 domains of otoferlin interact with $Ca_v1.3_S$ channels. Surprisingly, the *Otof*-C2-ACEF construct did not produce a significant recovery of the fast inactivating component of I_{Ca}. Notably this construct, contains a small deletion revealed by 3D structural modeling between the C2-E and C2-F (1695aar1731aa), which could alter the interaction with $Ca_v1.3$ channels.

Otoferlin and ultrafast endocytosis

A striking finding of our study was the expression of ultrafast endocytosis in auditory IHCs. Although different slow modes of endocytosis, likely clathrin dependent, have been described in IHCs (Beutner et al., 2001; Cho et al., 2011; Neef et al., 2014; Jung et al., 2015), they remain too slow to support the unusually high rate of exocytosis in auditory IHCs. Previous studies have revealed the existence of ultrafast endocytosis with a time constant of 50 ms in mouse hippocampal synapses (Watanabe et al., 2013b, 2014). The molecular mechanisms underlying ultrafast endocytosis are not fully understood, but its dependence on dynamin to pinch off the endocytic vesicle is well recognized. Consistent with these previous studies, we here report a novel dynamin-dependent ultrafast endocytosis in IHCs that can compensate exocytosis at a 20 ms time scale. This time scale is too fast for the dynamin-dependent clathrin-mediated endocytosis known to occur in IHCs at time scales ranging from 300 ms to 30 s, and we found that ultrafast endocytosis was absent in IHCs lacking otoferlin. We propose that otoferlin functions as a dual Ca^{2+} sensor for exocytosis and endocytosis, much like synaptotagmin I (Poskanzer et al., 2003; Yao et al., 2011).

Ultrafast endocytosis in neuronal synapses is sensitive to latrunculin-A, a sponge toxin that disrupts the F-actin filaments at synaptic active zones (Watanabe et al., 2013b). The F-actin cytoskeleton is thought to be essential for the polymerization and constriction of dynamin molecules around the membrane neck of the vesicles before fission and scission. Interestingly, latrunculin-A has also been shown previously to disrupt F-actin at the IHC ribbon active zones and increase the rate of exocytosis (Vincent et al., 2015; Guillet et al., 2016). We believe that increased exocytotic rates produced by latrunculin-A could also be, at least in part, due to inhibi-

tion of ultrafast endocytosis, resulting in a positive effect on exocytosis similar to that observed with Dyngo-4a.

Conclusions

Our study shows the importance of the C-terminal C2 domains of otoferlin in triggering RRP exocytosis and regulating ultrafast endocytosis in IHCs. However, these mini-otoferlins did not restore vesicle replenishment at the IHC active zones. This process possibly requires cooperative intramolecular interactions between C2 domains of otoferlin, similar to those of the tandem C2 domains of synaptotagmin-1 (Evans et al., 2016).

References

Akil O, Rouse SL, Chan DK, Lustig LR (2015) Surgical method for virally mediated gene delivery to the mouse inner ear through the round window membrane. J Vis Exp. Advance online publication. Retrieved March 16, 2015. doi: 10.3791/52187.

Azimzadeh JB, Fabella BA, Kastan NR, Hudspeth AJ (2018) Thermal excitation of the mechanotransduction apparatus of hair cells. Neuron 97:586–595.e4.

Beurg M, Michalski N, Safieddine S, Bouleau Y, Schneggenburger R, Chapman ER, Petit C, Dulon D (2010) Control of exocytosis by synaptotagmins and otoferlin in auditory hair cells. J Neurosci 30:13281–13290.

Beutner D, Voets T, Neher E, Moser T (2001) Calcium dependence of exocytosis and endocytosis at the cochlear inner hair cell afferent synapse. Neuron 29:681–690.

Bock G, Gebhart M, Scharinger A, Jangsangthong W, Busquet P, Poggiani C, Sartori S, Mangoni ME, Sinnegger-Brauns MJ, Herzig S, Striessnig J, Koschak A (2011) Functional properties of a newly identified C-terminal splice variant of Cav1.3 L-type Ca2+ channels. J Biol Chem 286:42736–42748.

Chapman ER (2008) How does synaptotagmin trigger neurotransmitter release? Annu Rev Biochem 77:615–641.

Chatterjee P, Padmanarayana M, Abdullah N, Holman CL, LaDu J, Tanguay RL, Johnson CP (2015) Otoferlin deficiency in zebrafish results in defects in balance and hearing: rescue of the balance and hearing phenotype with full-length and truncated forms of mouse otoferlin. Mol Cell Biol 35:1043–1054.

Cho S, Li GL, von Gersdorff H (2011) Recovery from short-term depression and facilitation is ultrafast and Ca2+ dependent at auditory hair cell synapses. J Neurosci 31:5682–5692.

Delvendahl I, Vyleta NP, von Gersdorff H, Hallermann S (2016) Fast, temperature-sensitive and clathrin-independent endocytosis at central synapses. Neuron 90:492–498.

Dulon D, Safieddine S, Jones SM, Petit C (2009) Otoferlin is critical for a highly sensitive and linear calcium-dependent exocytosis at vestibular hair cell ribbon synapses. J Neurosci 29:10474–10487.

Dulon D, Papal S, Patni P, Cortese M, Vincent PF, Tertrais M, Emptoz A, Tlili A, Bouleau Y, Michel V, Delmaghani S, Aghaie A, Pepermans E, Alegria-Prevot O, Akil O, Lustig L, Avan P, Safieddine S, Petit C, El-Amraoui A (2018) Clarin-1 gene transfer rescues auditory synaptopathy in model of Usher syndrome. J Clin Invest 128:3382–3401.

Duncker SV, Franz C, Kuhn S, Schulte U, Campanelli D, Brandt N, Hirt B, Fakler B, Blin N, Ruth P, Engel J, Marcotti W, Zimmermann U, Knipper M (2013) Otoferlin couples to clathrin-mediated endocytosis in mature cochlear inner hair cells. J Neurosci 33:9508–9519.

Emptoz A, Michel V, Lelli A, Akil O, Boutet de Monvel J, Lahlou G, Meyer A, Dupont T, Nouaille S, Ey E, Franca de Barros F, Beraneck M, Dulon D, Hardelin JP, Lustig L, Avan P, Petit C, Safieddine S (2017) Local gene therapy durably restores vestibular function in a mouse model of usher syndrome type 1G. Proc Natl Acad Sci U S A 114:9695–9700.

Evans CS, He Z, Bai H, Lou X, Jeggle P, Sutton RB, Edwardson JM, Chapman ER (2016) Functional analysis of the interface between the tandem C2 domains of synaptotagmin-1. Mol Biol Cell 27:979–989.

Fuson KL, Montes M, Robert JJ, Sutton RB (2007) Structure of human synaptotagmin 1 C2AB in the absence of Ca^{2+} reveals a novel domain association. Biochemistry 46:13041–13048.

Guillet M, Sendin G, Bourien J, Puel JL, Nouvian R (2016) Actin filaments regulate exocytosis at the hair cell ribbon synapse. J Neurosci 36:649–654.

Hams N, Padmanarayana M, Qiu W, Johnson CP (2017) Otoferlin is a multivalent calcium-sensitive scaffold linking SNAREs and calcium channels. Proc Natl Acad Sci U S A 114:8023–8028.

Han W, Rhee JS, Maximov A, Lin W, Hammer RE, Rosenmund C, Südhof TC (2005) C-terminal ECFP fusion impairs synaptotagmin 1 function: crowding out synaptotagmin 1. J Biol Chem 280:5089–5100.

Harsini FM, Chebrolu S, Fuson KL, White MA, Rice AM, Sutton RB (2018) FerA is a membrane-associating four-helix bundle domain in the ferlin family of membrane-fusion proteins. Sci Rep 8:10949.

Jung S, Maritzen T, Wichmann C, Jing Z, Neef A, Revelo NH, Al-Moyed H, Meese S, Wojcik SM, Panou I, Bulut H, Schu P, Ficner R, Reisinger E, Rizzoli SO, Neef J, Strenzke N, Haucke V, Moser T (2015) Disruption of adaptor protein 2μ (AP-2μ) in cochlear hair cells impairs vesicle reloading of synaptic release sites and hearing. EMBO J 34:2686–2702.

Kiang N (1965) Discharge patterns of single fibers in the cat's auditory nerve. Cambridge, MA: MIT.

Lek A, Evesson FJ, Sutton RB, North KN, Cooper ST (2012) Ferlins: regulators of vesicle fusion for auditory neurotransmission, receptor trafficking and membrane repair. Traffic 13:185–194.

Lek A, Evesson FJ, Lemckert FA, Redpath GM, Lueders AK, Turnbull L, Whitchurch CB, North KN, Cooper ST (2013) Calpains, cleaved mini-dysferlinC72, and L-type channels underpin calcium-dependent muscle membrane repair. J Neurosci 33:5085–5094.

Liberman MC (2017) Noise-induced and age-related hearing loss: new perspectives and potential therapies. F1000Res. 6:927.

Lindau M, Neher E (1988) Patch-clamp techniques for time-resolved capacitance measurements in single cells. Pflugers Arch 411:137–146.

Llanga T, Nagy N, Conatser L, Dial C, Sutton RB, Hirsch ML (2017) Structure-based designed nano-dysferlin significantly improves dysferlinopathy in BLA/J mice. Mol Ther 25:2150–2162.

Meyer AC, Frank T, Khimich D, Hoch G, Riedel D, Chapochnikov NM, Yarin YM, Harke B, Hell SW, Egner A, Moser T (2009) Tuning of synapse number, structure and function in the cochlea. Nat Neurosci 12:444–453.

Michalski N, Goutman JD, Auclair SM, Boutet de Monvel J, Tertrais M, Emptoz A, Parrin A, Nouaille S, Guillon M, Sachse M, Ciric D, Bahloul A, Hardelin JP, Sutton RB, Avan P, Krishnakumar SS, Rothman JE, Dulon D, Safieddine S, Petit C (2017) Otoferlin acts as a Ca2+ sensor for vesicle fusion and vesicle pool replenishment at auditory hair cell ribbon synapses. Elife 6:e31013.

Moreno CM, Dixon RE, Tajada S, Yuan C, Opitz-Araya X, Binder MD, Santana LF (2016) Ca(2+) entry into neurons is facilitated by cooperative gating of clustered Cav1.3 channels. Elife 5:e15744.

Moser T, Beutner D (2000) Kinetics of exocytosis and endocytosis at the cochlear inner hair cell afferent synapse of the mouse. Proc Natl Acad Sci U S A 97:883–888.

Moser T, Neef A, Khimich D (2006) Mechanisms underlying the temporal precision of sound coding at the inner hair cell ribbon synapse. J Physiol 576:55–62.

Neef J, Jung S, Wong AB, Reuter K, Pangrsic T, Chakrabarti R, Kügler S, Lenz C, Nouvian R, Boumil RM, Frankel WN, Wichmann C, Moser T (2014) Modes and regulation of endocytic membrane retrieval in mouse auditory hair cells. J Neurosci 34:705–716.

Padmanarayana M, Hams N, Speight LC, Petersson EJ, Mehl RA, Johnson CP (2014) Characterization of the lipid binding properties of otoferlin reveals specific interactions between PI(4,5)P2 and the C2C and C2F domains. Biochemistry 53:5023–5033.

Palmer AR, Russell IJ (1986) Phase-locking in the cochlear nerve of the guinea-pig and its relation to the receptor potential of inner hair-cells. Hear Res 24:1–15.

Pangrsic T, Lasarow L, Reuter K, Takago H, Schwander M, Riedel D, Frank T, Tarantino LM, Bailey JS, Strenzke N, Brose N, Müller U, Reisinger E, Moser T (2010) Hearing requires otoferlin-dependent efficient replenishment of synaptic vesicles in hair cells. Nat Neurosci 13:869–876.

Poskanzer KE, Marek KW, Sweeney ST, Davis GW (2003) Synaptotagmin I is necessary for compensatory synaptic vesicle endocytosis *in vivo*. Nature 426:559–563.

Ramakrishnan NA, Drescher MJ, Drescher DG (2009) Direct interaction of otoferlin with syntaxin 1A, SNAP-25, and the L-type voltage-gated calcium channel Cav1.3. J Biol Chem 284:1364–1372.

Ramakrishnan NA, Drescher MJ, Morley BJ, Kelley PM, Drescher DG (2014) Calcium regulates molecular interactions of otoferlin with soluble NSF attachment protein receptor (SNARE) proteins required for hair cell exocytosis. J Biol Chem 289:8750–8766.

Redpath GM, Woolger N, Piper AK, Lemckert FA, Lek A, Greer PA, North KN, Cooper ST (2014) Calpain cleavage within dysferlin exon 40a releases a synaptotagmin-like module for membrane repair. Mol Biol Cell 25:3037–3048.

Revelo NH, Kamin D, Truckenbrodt S, Wong AB, Reuter-Jessen K, Reisinger E, Moser T, Rizzoli SO (2014) A new probe for super-resolution imaging of membranes elucidates trafficking pathways. J Cell Biol 205: 591–606.

Roux I, Safieddine S, Nouvian R, Grati M, Simmler MC, Bahloul A, Perfettini I, Le Gall M, Rostaing P, Hamard G, Triller A, Avan P, Moser T, Petit C (2006) Otoferlin, defective in a human deafness form, is essential for exocytosis at the auditory ribbon synapse. Cell 127:277–289.

Safieddine S, Wenthold RJ (1999) SNARE complex at the ribbon synapses of cochlear hair cells: analysis of synaptic vesicle- and synaptic membrane-associated proteins. Eur J Neurosci 11:803–812.

Scharinger A, Eckrich S, Vandael DH, Schönig K, Koschak A, Hecker D, Kaur G, Lee A, Sah A, Bartsch D, Benedetti B, Lieb A, Schick B, Singewald N, Sinnegger-Brauns MJ, Carbone E, Engel J, Striessnig J (2015) Cell-type-specific tuning of Cav1.3 Ca(2+)-channels by a C-terminal automodulatory domain. Front Cell Neurosci 9:309.

Selvakumar D, Drescher MJ, Deckard NA, Ramakrishnan NA, Morley BJ, Drescher DG (2017) Dopamine D1A directly interacts with otoferlin synaptic pathway proteins: Ca^{2+} and phosphorylation underlie an NSF-to-AP2mu1 molecular switch. Biochem J 474:79–104.

Shen J, Scheffer DI, Kwan KY, Corey DP (2015) SHIELD: an integrative gene expression database for inner ear research. Database (Oxford) 2015:bav071.

Südhof TC (2012) Calcium control of neurotransmitter release. Cold Spring Harb Perspect Biol 4:a011353.

Taberner AM, Liberman MC (2005) Response properties of single auditory nerve fibers in the mouse. J Neurophysiol 93:557–569.

Vincent PF, Bouleau Y, Safieddine S, Petit C, Dulon D (2014) Exocytotic machineries of vestibular type I and cochlear ribbon synapses display similar intrinsic otoferlin-dependent Ca2+ sensitivity but a different coupling to Ca2+ channels. J Neurosci 34:10853–10869.

Vincent PF, Bouleau Y, Petit C, Dulon D (2015) A synaptic F-actin network controls otoferlin-dependent exocytosis in auditory inner hair cells Elife 4:e10988.

Vincent PF, Bouleau Y, Charpentier G, Emptoz A, Safieddine S, Petit C, Dulon D (2017) Different $Ca_V1.3$ channel isoforms control distinct components of the synaptic vesicle cycle in auditory inner hair cells. J Neurosci 37:2960–2975.

Vogl C, Panou I, Yamanbaeva G, Wichmann C, Mangosing SJ, Vilardi F, Indzhykulian AA, Pangršič T, Santarelli R, Rodriguez-Ballesteros M, Weber T, Jung S, Cardenas E, Wu X, Wojcik SM, Kwan KY, Del Castillo I, Schwappach B, Strenzke N, Corey DP, et al. (2016) Tryptophan-rich basic protein (WRB) mediates insertion of the tail-anchored protein otoferlin and is required for hair cell exocytosis and hearing. EMBO J 35:2536–2552.

von Gersdorff H, Matthews G (1994a) Dynamics of synaptic vesicle fusion and membrane retrieval in synaptic terminals. Nature 367:735–739.

von Gersdorff H, Matthews G (1994b) Inhibition of endocytosis by elevated internal calcium in a synaptic terminal. Nature 370:652–655.

Wang S, Li Y, Ma C (2016) Synaptotagmin-1 C2B domain interacts simultaneously with SNAREs and membranes to promote membrane fusion. Elife 5:e14211.

Watanabe S, Liu Q, Davis MW, Hollopeter G, Thomas N, Jorgensen NB, Jorgensen EM (2013a) Ultrafast endocytosis at caenorhabditis elegans neuromuscular junctions. Elife 2:e00723.

Watanabe S, Rost BR, Camacho-Pérez M, Davis MW, Söhl-Kielczynski B, Rosenmund C, Jorgensen EM (2013b) Ultrafast endocytosis at mouse hippocampal synapses. Nature 504:242–247.

Watanabe S, Trimbuch T, Camacho-Pérez M, Rost BR, Brokowski B, Söhl-Kielczynski B, Felies A, Davis MW, Rosenmund C, Jorgensen EM (2014) Clathrin regenerates synaptic vesicles from endosomes. Nature 515: 228–233.

Yamashita T, Eguchi K, Saitoh N, von Gersdorff H, Takahashi T (2010) Developmental shift to a mechanism of synaptic vesicle endocytosis requiring nanaodomain Ca^{2+}. Nat Neurosci 13:838–844.

Yao J, Kwon SE, Gaffaney JD, Dunning FM, Chapman ER (2011) Uncoupling the roles of synaptotagmin I during endo- and exocytosis of synaptic vesicles. Nat Neurosci 15:243–249.

Yasunaga S, Grati M, Cohen-Salmon M, El-Amraoui A, Mustapha M, Salem N, El-Zir E, Loiselet J, Petit C (1999) A mutation in OTOF, encoding otoferlin, a FER-1-like protein, causes DFNB9, a nonsyndromic form of deafness. Nat Genet 21:363–369.

Yasunaga S, Grati M, Chardenoux S, Smith TN, Friedman TB, Lalwani AK, Wilcox ER, Petit C (2000) OTOF encodes multiple long and short isoforms: genetic evidence that the long ones underlie recessive deafness DFNB9. Am J Hum Genet 67:591–600.